FU Berlin
Department of Mathematics and Computer Science
Master's Program in Bioinformatics
and
International Max Planck Research School for Computational Biology and Scientific Computing

Master's Thesis

Investigation of the reaction-diffusion processes of rod cell disc membrane photoactivation with single-particle resolution

submitted by

Johannes Seibert

on 8th December 2010

Supervisor

Dr. Frank Noé

Reviewers

Dr. Frank Noé
Prof. Dr. Christof Schütte

Statement

I hereby confirm that this thesis is my own work and that I have documented all sources used.

Johannes Seibert

Berlin, 8th December 2010

Acknowledgements

First of all I would like to thank Dr. Frank Noé. He gave me the opportunity to work on this interesting topic and supported me with multiple hours of his valuable advices in all biophysical, mathematical and computational issues that I came across during this work.

In the same manner I would also like to thank our collaborator at the Charité Berlin Dr. Martin Heck who did the experiments and provided us with the data on which this study is based. It were also multiple hours in which he teached me the biological details of the system that we wanted to simulate. Thanks a lot also for that.

The third person that I want to thank is my fiancée Susanne. Without her continuous support and motivation I would likely have refused to go on after these many dead ends in which I got stuck during my research from time to time.

Finally I would like to thank all people in the Computational Molecular Biology group, especially my roommate Martin Held and also Martin Senne who implemented a first algorithm for a particle dynamics simulator which I could use as a starting point for this project.

Investigation of the reaction-diffusion processes of rod cell disc membrane photoactivation with single-particle resolution

December 8, 2010

Abstract

Rod cell phototransduction is a prime example of a functional module whose properties may strongly depend on its specific spatial embedding. The rod outer segment has a highly regular layered geometry comprising disc membranes that are densely filled with the photo-collecting Rhodopsins and their G-proteins Transducin. Despite a wealth of functional studies on rod cell phototransduction and a rather complete knowledge of the proteins involved in the process, the spatiotemporal mechanism of the activation cascade is poorly understood. Since recently, the existence of Rhodopsin patterns on the disc and their possible effects on functional properties of photoactivation are highly debated. In the present study we conduct spatiotemporal simulations of the two-dimensional reaction-diffusion photoactivation processes on the disc membrane with all protein copies explicitly resolved. We investigate the effects of crowding, the spatiotemporal evolution of the activation, and different settings of the reaction rates of the physicochemical events such as the dissociation of G-protein subunits. Finally, we compare free diffusion of the involved proteins with a situation where attractive interactions favor Rhodopsin-Rhodopsin aggregations. In order to compare our results to a well-defined experimental test system, the simulations are set up on a spherical membrane mimicking experimentally prepared disc membrane vesicles for which extensive kinetic studies exist. Our analyses yield insight into which space-time mechanisms in the phototransduction activation module are possible and allow a number of highly debated questions concerning microscopic rate constants, pattern formation on the disc membrane, and sources of the single-photon response uniformity to be reconsidered.

Contents

1 Introduction

A cellular module is a functional unit of interacting molecules that goes through cycles to perform specific task for the cell [28]. The functionality of modules and entire cascades has classically been understood in terms of reaction networks, comprising the players (proteins, RNA, co-factors, ions, etc) and their interactions (reactions, aggregations). Recent years have seen increasingly many studies suggesting that spatial effects such as crowding or space exclusion at membranes, localization in the specific geometry of the cell, and the specific nature of the transport processes between these localizations play a perhaps equally important role in determining function. This is clear for molecules that exist in very low copy numbers, such as RNA [15] or activated Rhodopsin in the dim-light regime [46], where transport processes may become rate-limiting. Even when copy numbers are rather large, spatial effects, ranging from patterns of few molecules [20] to the macroscopic cell geometry [2, 6] may be determining modular function. Such spatial information is not contained in classical reaction networks and adds an important dimension to understanding modular function [45, 48, 2, 10, 6].

1.1 Rod cell phototransduction

As a guiding example, we consider the phototransduction module in the rod cell that comprises the entire signaling cascade and consists of sub-modules responsible for activation, shutoff, etc [28]. The rod cell phototransduction is the first step in dark vision, and is well understood in terms of the relevant molecules and their interactions [40, 53, 39, 36]. Rod phototransduction is initiated by light activation of Rhodopsin molecules that densely populate the intracellular disc membrane stacks (Fig. 1a) which is then transduced along the disks via Transducin and PDE molecules (Fig. 1b), resulting in concentration changes of freely diffusing second messenger molecules, leading to closure of Ca^{2+} channels, in turn causing a decrease of the "circulating dark current" which acts as a neuronal output signal [35]. Despite this rather detailed knowledge of interactions, some key properties of the rod vision signal transduction are still highly debated, in particular the nature of the two-dimensional transport processes on the disk membrane, which were classically understood as ordinary two-dimensional isotropic diffusion [54, 14]. The first steps of the G protein mediated visual signal transduction module are suggested to be rate limited by the transport of Rhodopsin and Transducin along the disk [5]. As the disks are densely populated with proteins, mainly Rhodopsins, Transducins and PDE in ratios of roughly 100:10:1, transport properties could be strongly affected by crowding or formation of local patterns. Single molecule particle tracking experiments of fluorescently labeled Transducin C-terminal peptides [31] seem to indicate anomalous diffusion behavior that may be induced by alterations in Rhodopsin packing upon light activation. Wang et al. [52] have found evidence for lipid microdomains on the disc which seem to accelerate the diffusion of the activated G_α subunit of Transducin remarkably. AFM Experiments have found bands of Rhodopsin oligomers [21], [20] suggesting that Rhodopsin may be organized in

extended areas of paracrystalline racks and patches. These bands would strongly restrict the transport of Rhodopsins part of such oligomer bands, while they have been suggested to promote the signal transduction to Transducin that could slide along these bands [20], or to be part of a general control mechanism allowing sensitivity adaptation of the photoreceptor [23]. The physiological relevance of these experiments is highly debated, as the experimental setup itself could induce unnatural pattern formation [11]. Nevertheless, Rhodopsin has been shown to exist both in monomeric and dimeric forms in detergents [30]. In a simulation study using coarse-grained MD, it was found that Rhodopsins tend to oligomerize depending on lipid bilayer thickness and composition [42]. A Monte-Carlo simulation of disks supports that the existence of diffusion obstacles would strongly affect the overall transport on the disk [13]. It is conceivable that oligomeric patterns are only metastable, i.e. change dynamically, and are modulated by the activation state of Rhodopsin or by the presence of Transducin. This has not been studied in detail yet.

These combined findings emphasize the significance of how spatial effects influence module function. More specifically, how do local arrangements / patterns of molecules influence transport processes, and how do the properties of these transport processes when embedded in the specific cellular geometry, propagate to functional properties of modules or entire cascades? While experimental techniques are usually restricted to observing individual properties or interactions, such a general question calls for complex reasoning that may be guided by computer experiments. In computer experiments, spatial models of the molecules and their interaction in specific environments can be simulated in time, with all model properties being observable and useful to calculating experimentally-measurable properties. This connection to experiment is one the one hand necessary to validate computer model, on the other hand, the computer model can then provide a structural, mechanistic and dynamical explanation of experimental evidence. The present challenge is to setup computer models that can describe the rod cell from the level of detailed molecular interactions to the entire cell while still being computationally tractable.

1.2 Theoretical approaches to the system

In order to access module properties, transport across the entire disk membrane or even the entire rod cell must be calculated, which is not feasible with models that resolve details of individual proteins such as molecular dynamics. The standard approach for modeling reaction or metabolic networks is using ordinary differential equations (ODEs). Starting from defined initial conditions the ODE model describes the change of metabolites over time due to reactions between them [45, 12]. ODEs can be paired with Gillespie dynamics to simulate systems where particles with low copy numbers are involved rendering a model with continuous concentrations inadequate [22]. ODEs and Gillespie dynamics have been used to model rod cell phototransduction [25, 24, 36]. However, ODEs and Gillespie dynamics assume that the reaction container is well-stirred such that concentrations are homogeneous at all times, and do not resolve any spatial information [45]. Thus, these approaches

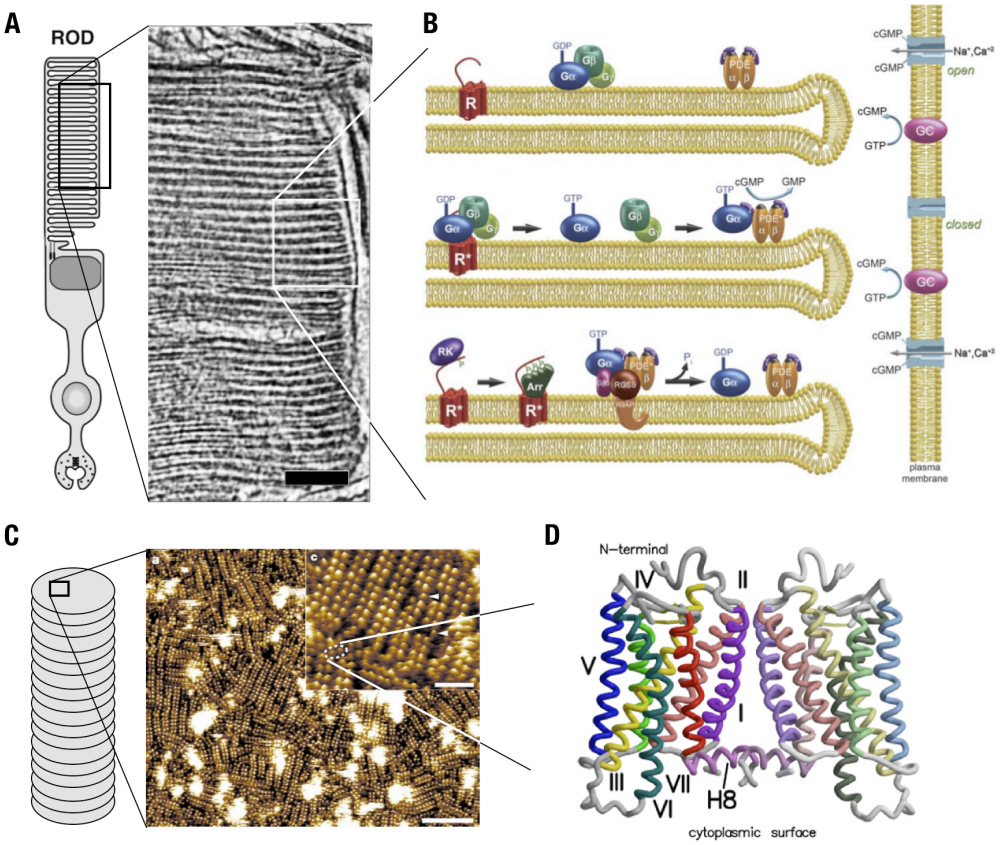

Figure 1: Overview over the different geometrical and signal transduction features of the rod cell. (A) Sketch of the rod cell [9] next to an electron tomogram of the rod outer segment, showing the layered disc geometry [38]. (B) Schematic of the Phototransduction Cascade Activation and Inactivation [8]. Upper disc: Illustration of inactive Rhodopsin (R), Transducin (Ga, Gb, and Gg subunits), and PDE (a, b, and g subunits) in the dark. Middle disc: Illustration of the light-induced cascade activation = Transducin and PDE activation. Lower disc: Illustration of the cascade inactivation = R* inactivation via phosphorylation by Rhodopsin kinase (RK) followed by Arrestin (Arr) binding and Transducin/PDE inactivation by the RGS9-1.Gb5.R9AP complex. The Guanylate cyclase (GC) is shown as a component of the plasma membrane; in real cells it is likely to be present within the disc membranes as well. (C) Sketch of the pile of discs next to an atomic-force microscopy topograph showing paracrystalline arrangements of Rhodopsin dimers [21] (D) Conformation of a Rhodopsin dimer in recently obtained crystals (PDB ID 2I35). The proteinprotein interactions in these dimers involve residues from helices I, II, and H-8, as well as the palmitoyl chains covalently bound to the protein.

are inadequate to address the present questions concerning the relevance of pattern formation, transport processes and specific geometry.

Two-dimensional lattice-based simulations of the disk membrane [33, 34, 17, 13] and three-dimensional reaction-diffusion simulations of the rod cell geometry [6, 10, 2] have been used to simulate rod phototransduction incorporating geometrical information. In a more general sense, compartment or subvolume-based simulation platforms exist, including Virtual Cell [49], MesoRD [26] and SmartCell [1]. While these approaches do provide mechanistic insight, they are still inadequate to model complex local and possibly dynamical patterns such as formation Rhodopsin oligomers [21] and realistic crowding behavior and some molecular processes, such as the initial randomness after single photon absorption [25, 24] or the generation of photocurrent following channel closure [6, 10, 2, 25, 24] need to be modeled with imposed empirical laws that cannot be easily validated on a microscopic level, nor do they yield a detailed understanding of the processes involved.

Such detail is resolved by models that explicitly describe the motion of individual particles in space and time. Several simulation platforms exist, including MCell [50], Smoldyn [3], CyberCell [7] and Cell++ [48] where the position of particles in space is propagated with diffusional dynamics and reaction-competent particles can react when being in close enough distance.

In the present study we use an algorithm, based on the time but not space discrete propagation of single particles and the evaluation of stochastic reactions between them, to simulate the two-dimensional reaction-diffusion processes of the two proteins that govern the initial steps in the primary Rod cell photoactivation cascade: Rhodopsin and the G-protein Transducin. We restrict our study to the case of single-photon activation and investigate the effects of crowding and assess the behavior of the process in different regimes in which either the system could be considered as well mixed and therefore be described by an ODE model or the system is governed by individual single particle events. Finally, we outline a possible method to compare free diffusion of the involved proteins with a situation where attractive interactions favor Rhodopsin-Rhodopsin aggregations. In order to compare our results to a well-defined experimental test system, the simulations are set up on a spherical membrane mimicking the disc membrane vesicles prepared in [27]. Our analyses yield insight into which space-time mechanisms in the phototransduction activation module are possible and allow a number of highly debated questions concerning pattern formation on the disc membrane to be reconsidered.

2 Experimental basis: Investigation of the rod cell disc membrane

The basis of this study is an experiment by M. Heck and K.P. Hofmann in which the first steps of the rod cell photoactivation cascade are studied in detail. The following section describes the biological system under investigation, the features and the geometry of the experimental setup and the results obtained by the experiment. For a more in-depth description please be also referred to the publication of the experiment: [27].

2.1 First steps in seeing

As already pointed out in the introduction, signal transduction in the rod cell starts with light induced activation of Rhodopsin molecules, being situated densely packed in thousands of copies on the surface of disc membranes. Once activated by a photon, Rhodopsin traverses multiple intermediate states, the most pronounced being MetaI, and eventually reaches an equilibrium between the MetaI and MetaII configuration from which the latter is capable of G-protein (G) activation, the subsequent activation reactions in the signal cascade.

Rhodopsin in MetaII configuration (R^*) forms a complex with G-proteins which induces a nucleotide exchange in the R^*-bound G-protein. In this exchange the protein bound low-energy GDP is exchanged by a high-energy GTP, rendering the G-protein to be in an active state (G^*). After R^*G^* complex dissociation R^* and G^* are released and R^* can continue to activate ground state G-proteins. The released G^* has a smaller membrane affinity than the G-protein in the ground state G. This change in membrane affinity is the key element of the applied experiment which uses kinetic light scattering to read out the number of G^* dissociating from the membrane. The following scheme gives an overview over all relevant reactions in the experiment:

$$MetaI \underset{k_{-1}}{\overset{k_1}{\rightleftharpoons}} MetaII(=R^*)$$

$$G_{GDP} + R^* \underset{k_{-2}}{\overset{k_2}{\rightleftharpoons}} G_{GDP}R \underset{k_{-3}(GDP)}{\overset{k_3(GDP)}{\rightleftharpoons}} G_0R^* \underset{k_{-4}(GTP)}{\overset{k_4(GTP)}{\rightleftharpoons}} G_{GTP}R^* \underset{k_{-5}}{\overset{k_5}{\rightleftharpoons}} G_{GTP} + R^*$$

$$G_{GTP} \underset{k_{-6}}{\overset{k_6}{\rightleftharpoons}} G_{GTP}(SOL)$$

The membrane binding reactions of already dissociated G^* and free G in solution are neglected here since they occur on too large time scales (in order of seconds) to be relevant for our simulations.

2.2 Experimental setup and disc vesicles

To investigate the system described above, Heck and Hofmann prepared bovine rod outher segments and hypotonically stripped off its disc membranes which, once in

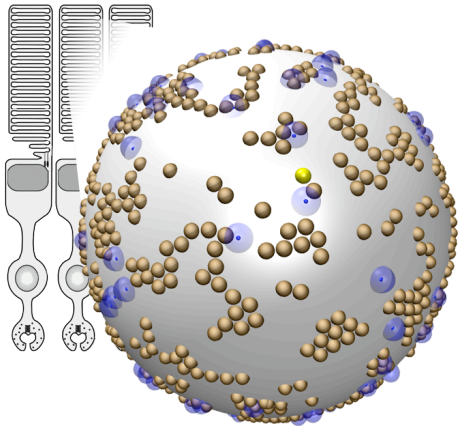

Figure 2: In the experiment of Heck and Hofmann, disc membranes are stripped off from the rod cells and form spherical shaped vesicles in buffer solution. In this image, besides G-proteins (blue) Rhodopsin oligomers (brown) are here assumed to be present on the disc membrane for illustration purposes. The question whether this structures are present on real disc membranes has been highly debated to date and could not been answered yet.

flat disc shape, take the form of a spherical vesicle in buffer solution, outside their cellular environment. See here also Figure 2 for an illustration.

Because Rhodopsin is an integral membrane protein it is not washed away by the purification steps to generate a solution of disc vesicles. This leads to a functional model system of a disc membrane in which no proteins of the visual cascade are present except Rhodopsin. Now a dynamic study was possible by adding controlled amounts of G-proteins and nucleotides to the system in order to resolve the underlying reaction mechanism and its kinetics.

2.3 Experimental results

Despite titrating the amount of nucleotides present in the system, Heck and Hofmann titrated also the amount of G-protein. The resulting cumulative signal of G^* dissociation events is depicted in Figure 3 and is characterised by a short delay followed by a constant increase and an eventual plateau formation on different levels indicating the respective initial amount of available G on the membranes. The different G-protein concentration for the different setups can be found in Table 1.

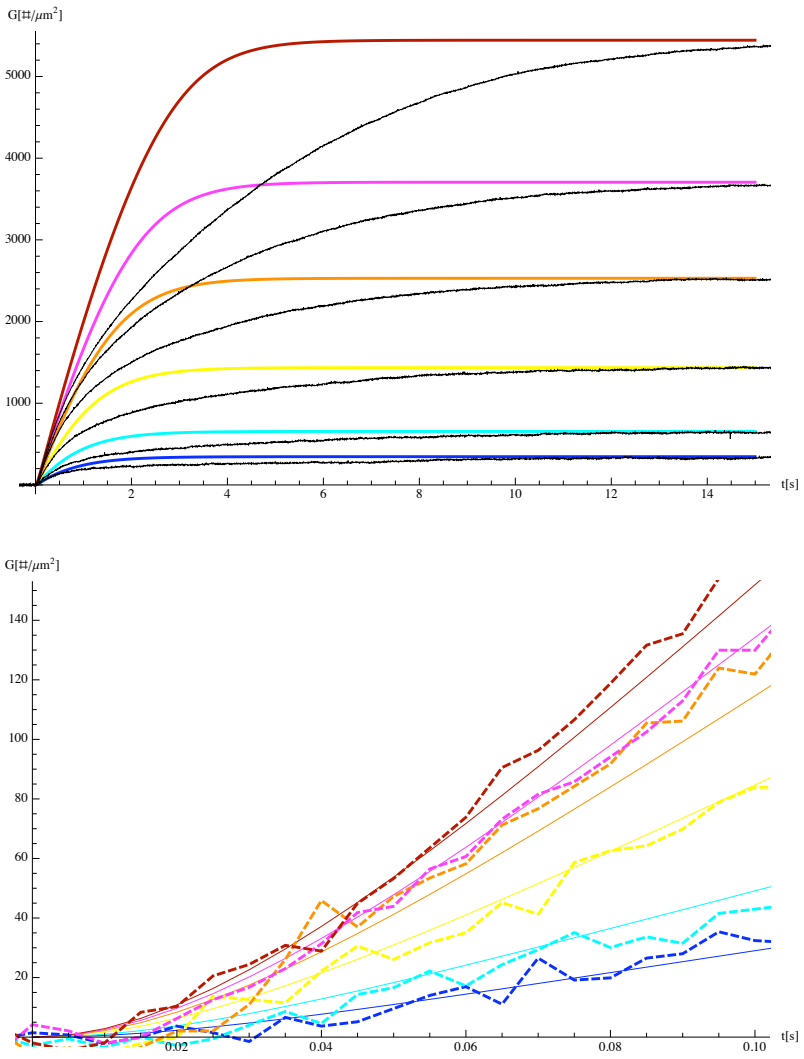

Figure 3: Experimental results and ODE model of the cumulative G^* production over time for different G concentrations. Color code of the setups: G10 blue, G20 cyan, G30 yellow, G40 orange, G50 magenta, G60 dark red. Upper plot: Complete trajectory of the experiment (black) and the ODE model results. Lower plot: Detail of the upper plot from 0 to 100ms. Dashed lines depict experimental results, straight lines ODE results.

	G10	G20	G30	G40	G50	G60
$[G]\mu m^2$	346	655	1436	2530	3706	5444

Table 1: Different G-protein concentrations used in the different experimental setups.

Symbol	Reaction	k
k_1	MetaI$\rightarrow$R*	28 s^{-1}
k_{-1}	MetaI$\leftarrow$R*	15 s^{-1}
k_2	R*+$G_{GDP}\rightarrow$R*G_{GDP}	0.53 $\frac{\mu m^2}{s}$
k_{-2}	R*+$G_{GDP}\longleftarrow$R*G_{GDP}	283 s^{-1}
$k_3(GDP)$	R*G_{GDP} $\overset{-GDP}{\longrightarrow}$ R*G_0	607.5 s^{-1}
$k_{-3}(GDP)$	R*G_{GDP} $\overset{+GDP}{\longleftarrow}$ R*G_0	2.22 $s^{-1} \times [GDP]$
$k_4(GTP)$	R*G_0 $\overset{+GTP}{\longrightarrow}$ R*G_{GTP}	2.6 $s^{-1} \times [GDP]$
$k_{-4}(GTP)$	R*G_0 $\overset{-GTP}{\longleftarrow}$ R*G_{GTP}	0 s^{-1}
k_5	R*$G_{GTP}\longrightarrow$R*+G*	48600 s^{-1}
k_{-5}	R*$G_{GTP}\longleftarrow$R*+G*	0 s^{-1}
k_6	G*$\longrightarrow\emptyset$	10000 s^{-1}
k_{-6}	G*$\longleftarrow\emptyset$	0 s^{-1}

Table 2: Reaction rate constants k from the ODE model of Heck and Hofmann.

A system of ordinary differential equations (ODE) was applied to learn the kinetic parameters of the involved reactions. Here they succeeded in simultaneously fitting their data by one set of kinetic parameters. The curves of the ODE description of the system can be found in Figure 3 and the resulting parameters are collected in Table 2. These parameters are the basis on which the reactions in our in silico simulation operate.

Our goal is to compare the results of our explicit reaction-diffusion particle dynamics simulation with the results of the ODE model as well as with the experimental results and highlight the differences that arise from the two modeling approaches with explicit particles on the one hand and assumed well stirred concentrations on the other.

3 Theory

In this section, the theoretical basis of the particle simulation approach is discussed.

3.1 Theoretical background

Biological systems are often described as reaction-diffusion processes of interacting chemical species. A traditional mathematical modelling approach to such processes is their description in terms of concentrations that are either space independent and evolve in time by using a system of ordinary differential equations (ODSs) or that are spatially dependend and evolve in time by using a system of partial differential equations (PDEs) [29]. However the use of concentrations has the limitation that it is only valid for very large numbers of molecules. If these numbers become smaller, e.g. there is only one activated Rhodopsin molecule that initiates the entire photoactivation cascade during single photon responses of Rod cells, their description in terms of a concentration can no longer be defined properly.

In such cases of low copy numbers it is necessary to give up the description in terms of concentrations and use discrete numbers of particles instead. The resulting algorithms are based on the stochastic Markov process that governs the dynamics of particle movements and reactions and are called stochastic simulation algorithms (SSAs).

There are two kinds of SSAs: The first subdivides the simulation volume artificially into small subvolumes [49, 26, 1]. Now particle movements in space are modelled as random jumps between these volumes and reactions are only considered possible within a subvolume that is assumed to be well mixed. The description of stochastic reactions based on discrete particle numbers in such a container is performed according to the Gillespie algorithm [22]. The disadvantage of this formalism is that is requires the assumption of well mixed parts in the system which limits the resolution in space and can therefore not be used for the modeling of single particle events.

The second kind of SSA is molecular based and simulates the trajectories of diffusive motion of individual molecules via stochastic differential equations (SDEs) [47]. Reactions between particles can occur if their distance is lower than the reaction radius and are performed with a probability defined in [22]. Algorithms of this kind include [50, 3, 7, 48].

Our approach is a derivative of this second kind of SSA. Due to the desired single particle resolution we do not discretize space and only dicretize time. Our system only involves diffusive Brownian motion of particles and reactions between them. Directed motion does not occur in our system.

The next sections describe in detail the used mathematical model for both particle diffusion and reaction threatment and their discretization in time.

3.2 Particle diffusion

Which is the correct equation for describing the diffusional motion of particles? A key modeling decision made here is that only some particles (which are of interest for the functional modules under investigation) are resolved. Thus, only a few particles will be explicitly described, while the presence of the nonresolved particles needs to enter the dynamical equations implicitly. This setting is covered by the Mori-Zwanzig formalism [55, 37], yielding a generalized Langevin equation, which describes particle motion subject to their interaction forces (repulsion at small distances and attraction for particles that tend to aggregate), friction, noise (due to random collisions with the nonresolved particles) and their history (neglecting particles creates memory effects). Furthermore, particles in fluids are subject to hydrodynamic forces which are due to long-range density correlations resulting from displacement of large particles (e.g. pressure waves).

In our model we make the following further assumptions:

1. We are interested in timescales long enough such that instantaneous particle velocities can be ignored (e.g. the velocity autocorrelation of liquid water decays within ∼500 fs [44], which is much faster than a single integration time step - see Sec. 4). This sets us in the overdamped limit, allowing the friction term in the Langevin equation to be dismissed.

2. We are interested in timescales long enough such that memory effects arising from neglecting the nonresolved particles have died out. This allows the memory term in the generalized Langevin equation to be dismissed.

3. Long-range density correlations (hydrodynamics) are relevant at the time- and length-scales interesting to us. However, the cell is crowded with particles of different sizes and forms, most of which are not resolved here. Treating hydrodynamics only amongst those particles resolved would result in an undesirable bias. We assume that these hydrodynamic contributions average out. Note that this assumption may be invalid in situations where there is a net transport in a region of the cell that would creates anisotropic hydrodynamic effects, e.g. motor proteins dragging vesicles along actin fibers.

4. Particles are treated as spheres. Molecules that strongly deviate from spherical form (such as fibers) need to be modeled as a collection of interacting spheres. This allows us to model the particle configuration based only on the positions of their centers (ignoring orientations), and to treat diffusion isotropically with a scalar diffusion coefficient.

Combining these assumptions leads to isotropic Brownian dynamics (also known as Smoluchowski or overdamped Langevin dynamics):

$$\frac{d\mathbf{x}(t)}{dt} = -\frac{\nabla V(\mathbf{x}(t))}{\gamma m} + \sqrt{\frac{2k_B T}{\gamma m}}\frac{d\boldsymbol{\eta}(t)}{dt}, \tag{1}$$

where $\mathbf{x}(t) \in \mathbb{R}^n$ is an n-dimensional vector indicating the instantaneous position of all n particles at time t, $d\mathbf{x}(t)/dt$ is change of these positions over time, $\nabla V(\mathbf{x}(t))$ is the gradient (spatial derivative) of the potential, γ is the friction, m the particle mass and the first term on the right hand side is the resulting deterministic force. The second term on the right hand side is a stochastic force where k_B is the Boltzmann constant, T is the temperature, k_BT is the thermal energy and $\boldsymbol{\eta}(t) \in \mathbb{R}^n$ is a n-dimensional Wiener process, i.e. each component is an independent random process with normally distributed increments $\eta(t_2) - \eta(t_1) \sim \mathcal{N}(0, t_2 - t_1)$. The fluctuation-dissipation theorem relates friction and temperature *via* the diffusion constant D:

$$D = \frac{kT}{\gamma m} \tag{2}$$

which allows Eq. (1) to be rewritten as:

$$\frac{d\mathbf{x}(t)}{dt} = -D\frac{\nabla V(\mathbf{x}(t))}{kT} + \sqrt{2D}\frac{d\boldsymbol{\eta}(t)}{dt}. \tag{3}$$

Due to the fluctuation-dissipation theorem, the diffusion constant is proportional with temperature (assuming that we are far away from a phase transition point), i.e. the diffusion constant can be parametrized at a given temperature:

$$D_{\text{ref}} = T_{\text{ref}}\frac{k}{\gamma m}$$

and based on this the diffusion constants at other temperatures can be obtained:

$$D(T) = \frac{T}{T_{\text{ref}}}D_{\text{ref}}.$$

The above equation is solved numerically by employing an Euler discretization with constant time step Δt, obtaining a discrete sequence of configurations in time, $\mathbf{x}_t$, related by:

$$\mathbf{x}_{t+\Delta t} = \mathbf{x}_t - \Delta t\, D\frac{\nabla V(\mathbf{x}(t))}{kT} + \sqrt{2D\Delta t}\boldsymbol{\eta}_t \tag{4}$$

where the noise is realized by independent normal variables $\boldsymbol{\eta}_t \sim [\mathcal{N}(0,1), ..., \mathcal{N}(0,1)]^T$. Δt needs to be chosen shorter than the smallest timescale of the system, i.e. it depends on the stiffness of the potential and on the diffusion constants. When Δt is sufficiently small, the Brownian Dynamics will, in absence of reactions, sample from the stationary distribution that is fully defined by the potential, Eq. (6). This fact is exploited in order to test the numerical correctness of the integration scheme.

3.3 Microscopic versus macroscopic diffusion

Two different concepts of diffusion constants exist, microscopic (model) diffusion constants D, and macroscopic diffusion constants D_{obs} which are usually those that are observable by experiments sensitive to particle motion. In order to understand

their relationship, let us first consider a single particle that does currently not interact with any other particle. Thus, the equation of motion for this particle is given by pure Brownian motion:

$$\frac{d\mathbf{x}(t)}{dt} = \sqrt{2D}\frac{d\boldsymbol{\eta}(t)}{dt}. \tag{5}$$

Assuming that our particle is at $\mathbf{x}(0) = \mathbf{0}$ initially and solving this equation for different realizations of the noise gives the probability distribution of finding the particle at a position $\mathbf{x}(t)$ at time t as:

$$\mathbf{x}(t) \sim \mathcal{N}(\mathbf{0}, 2Dt\,\mathbf{Id}),$$

i.e. a normal distribution with variance $2Dt$. Thus, the expected mean square displacement of the particle over time, defined by

$$\mathrm{msd}(t) = \langle(\mathbf{x}(0) - \mathbf{x}(t))^2\rangle$$

has two limits characterized by the characteristic times $t_1 < t_2$. At short times:

$$\mathrm{msd}(t < t_1) \approx 2Dt,$$

i.e. it increases linearly with time with slope $2D$. This is a characteristic behavior of diffusion and D is called the microscopic diffusion constant as it governs the motion of particles within their implicit media while neglecting the composition of the particle system, i.e. the interaction with other particles.

Now assume that the system is densely packed with particles that interact in some way (e.g. repulsion at small distances, but perhaps also other, additional forces). While on very short timescales, most particles may move freely with diffusion constant D, at longer timescales particles will bump into each other. Consequently, on long timescales the mean square displacement of particles will not grow with $2Dt$, but usually slower, because the particle motion is hindered by crowding. On long enough timescales, many such collision events will average out, again giving rise to an effective diffusional behavior. On these long timescales, the mean square displacement will also have the form

$$\mathrm{msd}(t > t_2) \approx 2D_{obs}t,$$

but now with a different effective diffusion D_{obs} that accounts for the composition and geometry of the system that the particle(s) of interest are moving in. Due to restrictions on size and timescale resolution, D_{obs} is usually the diffusion constant that can be obtained from experiments, while D is the diffusion constant used in a simulation model.

3.4 Reactions

Reactions are events which transform a number of nearby particles into other particles. Reactions in the sense of this simulator are not only chemical reactions, but

may have various physical realizations (including chemical reactions, conformational changes, aggregations, etc). We limit ourselves to uni- or bimolecular reactions, i.e. the types:

$$E \xrightarrow{k} P_1, ..., P_m$$

and

$$E_1 + E_2 \xrightarrow{k} P_1, ..., P_m$$

where E_1 and E_2 are "educts", i.e. the particles that are consumed by the reaction and P_i are the products, i.e. the particles that are created by the reaction. Reactions involving more than two educts can be modeled by splitting them up into multiple bimolecular reaction steps.

The reaction rate constant, k, expresses the fraction of the educts converted into products per time unit. Unimolecular reactions have a simple behavior. The products are produced with rate k, leading to the simple ordinary differential equations [4]:

$$\frac{dc_{P_1}(t)}{dt} = ... = \frac{dc_{P_m}(t)}{dt} = k\, c_E(t),$$

where c_x is the time-dependent concentration of particle type x. In unimolecular reactions, the reaction rate constant k represents a single-molecule event - it measures the inverse mean time needed for the educt to decay into the products. Thus, unimolecular reaction rate constants determined by experiments are identical to the microscopic reaction rate constants used in a model description.

The situation is more difficult for biomolecular reactions. The total rate, i.e. the total number of executions of the reaction per time unit of a bimolecular reaction taking place in a homogeneous reaction container is given by [4]:

$$\frac{dc_{P_1}(t)}{dt} = ... = \frac{dc_{P_m}(t)}{dt} = k\, c_{E_1}(t)\, c_{E_2}(t).$$

with $c_{E_1}(t)$ and $c_{E_2}(t)$ being the particle numbers of educts and k being the rate constant. In this macroscopic model, k hides many details that influence the reaction rate. In particular, for a reaction event to occur, one copy of E_1 and E_2 each must be in contact distance, such that the binding or aggregation event required for the reaction can take place. Once such an encounter or collision complex has been formed, there is subsequently a certain rate with which the two molecules will eventually overcome the chemical/physical reaction barrier. The first step, the encounter formation, happens *via* particle diffusion:

$$\overset{\text{separate molecules}}{E_1, E_2} \overset{\text{diffusional encounter}}{\longrightarrow} \overset{\text{encounter complex}}{E_1 : E_2} \overset{\text{activation}}{\longrightarrow} \overset{\text{products}}{P_1, ..., P_m}$$

In a particle simulation, the location and diffusional motion of each particle is explicit. We therefore need to distinguish the encounter and activation processes, as the motion leading to the encounter complex is directly simulated, and the activation can then only be conducted for those pairs of molecules that are close enough to

form an encounter complex. For each particle, a reaction radius R (see Table 3) is defined. When the inter-particle distance is smaller than the sum of reaction radii involved, we have an encounter complex:

$$d_{12} \leq R_{12} = R_1 + R_2.$$

The reaction radii are chosen based on physico-chemical intuition in order to represent a distance at which reaction partners are close enough such that their subsequent interaction is specific for this pair of molecules and can no longer be treated by a diffusional description in which the molecules may move independently. In other words, R_{12} may be regarded as the distance at which the interaction between these two molecules switches from a weak to a strong interaction. Changing this distance would change the encounter rate, and thus also change the activation rate needed to represent a given total reaction rate. Thus it is clear that the separation of the total rate constant into encounter and activation rate constants is not objective but is to some degree arbitrary, hence we use the convention that R_{12} is fixed first.

What is the activation rate constant needed in our model to reproduce a measured total rate constant k when a reaction distance R_{12} has been defined? We distinguish two types of reactions: Firstly, we consider a bimolecular reaction in three dimensions. For this, we assume a homogeneous mixture of particles of types E_1 and E_2, which freely diffuse with diffusion constants D_1 and D_2, form an encounter at distance R_{12} and then react with an activation rate k_a. The rate at which encounter complexes at distance R_{12} are formed is given by the Smoluchowski rate as

$$\frac{dc_{(E_1E_2)}(t)}{dt} = k_{enc} c_{E_1}(t)\, c_{E_2}(t)$$

with encounter rate constant

$$k_{enc} = 4\pi(D_{E_1} + D_{E_2})R_{12}.$$

Further taking into account that educts when having diffused into a distance of R_{12} are degraded with a rate k_a yields a total (macroscopic) rate that has an analogous form, but with a smaller effective radius (see [16] for derivation), given by:

$$k = 4\pi(D_{E_1} + D_{E_2}) \left(R_{12} - \sqrt{\frac{D_{E1} + D_{E2}}{k_a}} \tanh\left(R_{12} \sqrt{\frac{k_a}{D_{E_1} + D_{E_2}}} \right) \right).$$

thus, for a given measured k and our definition of R_{12}, k_a can be determined as the solution of this equation. However this derivation is only valid in three-dimensional geometry and is therefor not applicable to our system of membrane diffusion.

For this reason, using an analogous derivation (see 8.1), we derived a rate equation for biomolecular reactions taking place between educts diffusing on a two-dimensional surface (e.g. membrane proteins). This yields a total rate of:

$$k = 2\pi R_{12} \sqrt{D_{E1} + D_{E2}} \sqrt{k_a} \frac{I_1\left[R_{12}\sqrt{\frac{k_a}{D_{E_1}+D_{E_2}}}\right]}{I_0\left[R_{12}\sqrt{\frac{k_a}{D_{E_1}+D_{E_2}}}\right]},$$

where $I_\alpha[x]$ denotes the Modified Besselfunction of order α.

In the particle simulation, time is discretized into segments of Δt. The reaction rate must therefore be converted into a probability that the reaction will take place in a given time step. When making the assumption that a single particle cannot undergo multiple reactions in one time step (which is only true if the time step is sufficiently small compared to the reaction rates involved). The reaction probability is then obtained from the Poisson probability of finding at least one reaction event with rate k_a in a time window Δt [51]:

$$p(\Delta t) = 1 - \exp(-k_a \, \Delta t).$$

3.5 Interaction potentials and stationary distributions

Inter-particle potentials are useful for modeling space exclusion (e.g. crowding effects), reversible protein aggregations and correlation of particle motions due to electrostatic interactions. The potential assigns a potential energy to a particle configuration $\mathbf{x}(t)$, here denoted by $V(\mathbf{x}(t)) : \mathbb{R}^n \to \mathbb{R}$. Note that both the terms active in V and the length of the position vector $\mathbf{x}$ will change over time because of particle reactions which change the particle composition of the system. However, in between two reaction events, V is unique and during this time, the potential has an associated stationary density given by

$$p(\mathbf{x}) = Z^{-1} \exp\left(-\frac{V(\mathbf{x})}{k_B T}\right) \tag{6}$$

where $Z = \int_{\mathbf{x}} \exp\left(-\frac{V(\mathbf{x})}{k_B T}\right)$ is the partition function. In many real simulations, $p(\mathbf{x})$ will not be sampled from because of the reactions taking place that drive the system out of equilibrium. However, $p(\mathbf{x})$ is useful to parametrize the particle interactions in regimes where it can approach equilibrium (e.g. disc membranes in the dark equilibrated state). Since $p(\mathbf{x})$ is a stationary property of $V(\mathbf{x})$, we can also use it as a reference to evaluate the numerical correctness of the particle dynamics in the absence of reactions. $p(\mathbf{x})$ is useful to calculate all kinds of stationary properties, for example the radial distribution function between particles of set I with those of set J, defined by the ensemble average:

$$p(d) = \int_{\mathbf{x}} d\mathbf{x} \, p(\mathbf{x}) \sum_{i \in I} \sum_{j \in J} \delta(|\mathbf{x}_i - \mathbf{x}_j| - d), \tag{7}$$

where $\mathbf{x}_i$ and $\mathbf{x}_j$ are the subvectors of $\mathbf{x}$ describing the locations of particles i and j. This density is in practice approximated with a histogram obtained from a set of configurations at time-steps T:

$$p(d) \approx \frac{|\{(i,j,t) \;\mid\; ||\mathbf{x}_i(t) - \mathbf{x}_j(t)| - d| < \Delta d/2, \; i \in I, \; j \in J \, , t \in T\}|}{N_T N_I N_J}. \tag{8}$$

3.6 Markov chain Monte Carlo sampling scheme for probing the stationary distribution of a particle composition

In absence of reactions, the particle composition will not change and the only dynamical process in the system is diffusion of particles driven by thermal motion. This dynamics is in equilibrium, i.e. it has a well-defined stationary distribution given only by the potential, Eq. (6). In order to have an independent reference to test the implementation of our dynamics, we specify a Monte Carlo (MC) procedure for sampling $p(\mathbf{x})$:

Algorithm 1 Monte Carlo sampling scheme for the stationary distribution.

1. Start with time $t = 0$, an initial particle configuration $\mathbf{x}_{t=0}$ and an initial energy $E_{t=0}$ of $\mathbf{x}_{t=0}$.

2. Repeat for N steps (total simulation time of $N\Delta t$):

   (a) For each particle p with position x_t^p generate a new random position $\hat{x_t^p}$ with $x_t^p - \hat{x_t^p} \in [0, \sqrt{2D_p\Delta t}]$. This displacement scheme mimicks Brownian motion of particles to be more comparable to our Brownian dynamics simulator. Any other random displacement would also be valid for the MC algorithm.

   (b) Compute the energy E_t' of the new configuration $\mathbf{x}_t' = \mathbf{x}_t \backslash \{x_t^p\} \cup \{\hat{x_t^p}\}$ using the particle repulsion potentials and compute $\Delta E_t = E_t' - E_t$.

   (c) Accept the new particle position with probability $min\left[1, exp(\frac{\Delta E_t}{k_B T})\right]$ with Boltzmann constant k_B and temperature T.

3.7 Choosing the appropriate coordinate system

The experimental setup of Heck and Hofmann [27] renders the former flat two dimensional disc membranes of Rod cells to become disc vesicles of near spherical shape. This makes the description of the reaction-diffusion system more difficult because of this special geometry but also more interesting because e.g. there exist no borders on the surface of a sphere. However the mathematical and algorithmitcal approaches to that problem have to be different from those describing ordinary two dimensional diffusion on a plane.

It would be possible to describe spherical diffusion and reactions by a setup simulating all three space dimensions and subjecting particles to potentials that force them to reside in a specified area (here the surface of a sphere). Such an implementation would have computational complexity $O(n^3)$. Though in this setup the implementation itself would be straight forward its efficiency would be rather low because the volume necessary to incorporate the simulated sphere would be almost completely empty and much computation power would be wasted by simulating vacuum.

The solution to this problem is the usage of a spherical coordinate system that defines a point p in space via its distance from the origin $r \in$, its inclination $\theta \in [0, \pi]$ and its azimuth $\phi \in [0, 2\pi]$; $p = (r, \theta, \phi)$ (see Figure 4). Since the size of a vesicle is fixed during a simulation and all particles reside on the vesicle surface, r is fixed for every particle. So a particle is defined by only two degrees of freedom; $p = (\theta, \phi)$ wich would reduce the computational order to $O(n^2)$ and exclusively describes the area on the vesicle surface. On the other hand the implementation, especially the neighborhood calculations becomes more complicated which will be described in the following sections.

Coordinate system conversions

In the following, the functions for coordinate transformations between the spherical and the Cartesian coordinate systems are briefly stated. (r, θ, ϕ) and (x, y, z) refer to the spherical and the Cartesian representations of the same point respectively. It is assumed, that both systems have the same origin.

Cartesian to spherical coordinates

$$\begin{aligned} r &= \sqrt{x^2 + y^2 + z^2} \\ \theta &= cos^{-1}(\frac{z}{r}) \\ \phi &= tan^{-1}(\frac{y}{x}) \end{aligned}$$

spherical to Cartesian coordinates

$$\begin{aligned} x &= r\ sin\,\theta\ cos\,\phi \\ y &= r\ sin\,\theta\ sin\,\phi \\ z &= r\ cos\,\theta \end{aligned}$$

3.7.1 Distance calculations on a sphere

The computation of distances between particles is essential for the simulation algorithm. All particle-particle interactions e.g. particle repulsion and also all reactions are based on that. Having given two particle positions in their spherical representations, $p_1 = (\theta_1, \phi_1)$, and $p_2 = (\theta_2, \phi_2)$, the distance between v and w can be computed via the spherical law of cosines

$$cos\,c = cos\,a\,cos\,b + sin\,a\,sin\,b\,cos\,C.$$

This law applies for a spherical triangle between three points on a sphere. Together with the north pole $n = (0, 0)$, p_1 and p_2 constitute such a spherical triangle. For the further derivation we follow the nomenclature of Figure 5: $n \mathrel{\widehat{=}} u$, $v \mathrel{\widehat{=}} p_1$

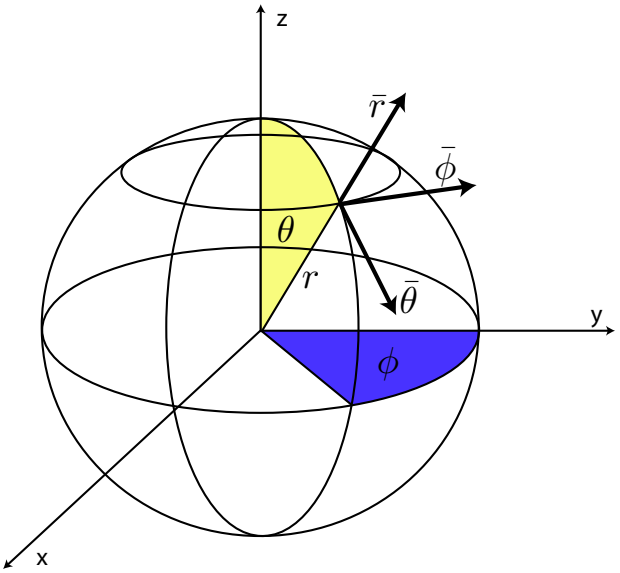

Figure 4: The spherical coordinate system. Point $p = (r, \theta, \phi)$ is defined by its distance from the origin r, its inclination θ between the x-z axis and its azimuthal angle ϕ between the x-y-axis. The unit vectors in point p: $\bar{r}, \bar{\theta}, \bar{\phi}$ are illustrated as well. Rotations around these vectors leave the name giving coordinate unchanged e.g. rotation around $\bar{\phi}$ leaves the ϕ value of the points unchanged.

and $w \mathrel{\widehat{=}} p_2$. So we want to compute the distance c between the two particles v and w.

Using the formula above we need the distance a, between u and v and distance b, between u and w. Since u is the north pole, a and b are given by arc length between the north pole and the respective particle coordinates v and w, which are just their θ-values multiplied by the radius of the sphere r:

$$a = r\theta_1, \; b = r\theta_2.$$

The unknown variable left is the angle C between the vertices a and b of the spherical triangle. These are also known when we define u to be the north pole:

$$C = min(abs(\phi_1 - \phi_2), \; 2\pi \; - abs(\phi_1 - \phi_2)).$$

The min in the formula handles the 2π periodicity in azimuthal spherical coordinates and prevents the reflex angle from being used. Excluding the reflex angle introduces a maximal boundary of distances between two points of half the circumference of the circle on the sphere defined by the two points. Larger distances on a sphere are naturally not possible since an increase in distance in one direction would decrease it in the other direction around the sphere.

Finally applying the inverse of the cosine we are left with the following formula to compute the distance between two points on the surface of a sphere:

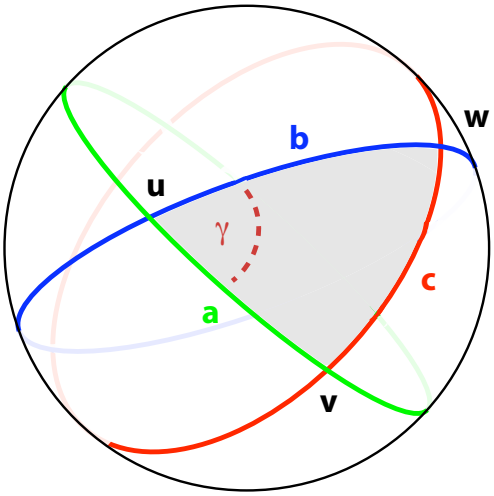

Figure 5: Illustration of the spherical law of cosines.

$$c = acos[cos\ a\ cos\ b + sin\ a\ sin\ b\ cos\ C]$$

4 In silico model and particle simulation

Our model consists of the two-dimensional diffusional motion of Rhodopsin and the G-protein Transducin on a vesicle (as extracted from a disc membrane [27]) and the primary phototransduction reactions between them. Table 3 lists the particle species included in the model.

Symbol	$D/\frac{\mu m^2}{s}$	$D_{obs}/\frac{\mu m^2}{s}$	R_c/nm	R/nm
	Rhodopsin			
R	0.95	0.7 [43]	1.745 PDB: 2I36	2.29
	Light-activated Rhodopsin (not G activation capable)			
MetaI	0.95	0.7 [43]	1.745 PDB: 2I37	2.29
	Light-activated Rhodopsin(G activation capable)			
MetaII (R^*)	0.95	0.7 [43]	1.745 PDB: 2I37	2.29
	Transducin			
G	1.63	1.3 [43]	0.58 ($R_c^{out} = 3.0$) PDB: 1GOT	$0,58$
	Activated Transducin (output)			
G^*	1.63	1.3 [43]	0.58 ($R_c^{out} = 3.0$) PDB: 1GOT	$0,58$
	Activated Rhodopsin - Transducin complex (GDP bound)			
R^*G_{GDP}	0.95	0.7 (same as R)	2.0 ($R_c^{out} = 3.0$) PDB: 1GOT+2I37	3.0
	Activated Rhodopsin - Transducin complex (empty state)			
R^*G_0	0.95	0.7 (same as R)	2.0 ($R_c^{out} = 3.0$) PDB: 1GOT+2I37	3.0
	Activated Rhodopsin - Transducin complex (GTP bound)			
R^*G_{GTP}	0.95	0.7 (same as R)	2.0 ($R_c^{out} = 3.0$) PDB: 1GOT+2I37	3.0

Table 3: Simulated Particles. D: microscopic diffusion constant that enters the dynamical equations, D_{obs}: observed macroscopic diffusion constant arising from diffusion in a crowded environment, R_c: intrinsic collision radius, R: intrinsic reaction radius. All diffusion constants are measured at $22°C$.

The simulation model propagates the positions and states of the particles involved in discrete time steps. In each time step, it performs two actions (1) diffusion of the different particle species in a potential and (2) reactions between them. Starting with an initial particle configuration, the simulation algorithm integrates the Brownian dynamics equation of motion subjected to an interaction potential

between particles (see Sections 4.2). In our case, this potential is a pair potential which only depends on particle distances $d_{ij} = |\mathbf{x}_i - \mathbf{x}_j|$ of pairs of particles i,j. It contains repulsive terms to avoid overlap of particles, and attractive terms to model protein aggregation.

Besides this particle movement, in every time step, the algorithm considers all reactions that are possible for each particle, chooses a reaction according to its rate constant and performs it with a certain probability (see Sec. 4.3).

In summary, the simulation algorithm can be outlined as given in Algorithm 2, the implementation and parametrization of particle diffusion and reactions are described subsequently.

Algorithm 2 Particle simulation algorithm

1. Start with time $t = 0$, an initial particle configuration $\mathbf{x}_{t=0}$ and corresponding pairwise distances $d_{ij} = |\mathbf{x}_{t,i} - \mathbf{x}_{t,j}|$.

2. Repeat for N steps (total simulation time of $N\Delta t$):

   (a) Advance the Brownian dynamics by one step of length Δt based on the interaction potential determined by the pairwise distances d_{ij} (see Table 4) and the particle type dependent diffusion constants D (see Table 3).

   (b) Create a list of reactions that can occur (see Sec. 4.3 and Table 5). For each particle that can react, choose a reaction with probability depending on its rate constant and execute the reaction with probability $p = 1 - \exp(-k_a\,\Delta t)$.

   (c) Update pairwise distances d_{ij}.

4.1 Particle diffusion on a sphere

As already explained in Section 3.2 , particle diffusion subjected to a potential can be simulated numerically via the following equation:

$$\mathbf{x}_{t+\Delta t} = \mathbf{x}_t - \Delta t\, D\frac{\nabla V(\mathbf{x}(t))}{kT} + \sqrt{2D\Delta t}\boldsymbol{\eta}_t$$

It states, that the particle position in the next timestep $x_{t+\Delta t}$ depends on the current position plus a potential and a noise contribution. Their computation in spherical geometry is explained in the following.

4.1.1 Potential contributions

The potentials regarded in our system are particle pair potentials that depend on pairwise distances. In Cartesian coordinates it would be straight forward to compute the change in distance according to the potential since the Cartesian coordinate system is space conserving. For example if one adds the perturbation vector $(1, 1)$

once to the origin and once to the vector $(10, 10)$, the resulting perturbation from the original point is in both cases the same namely $|(1, 1)|=\sqrt{2}$. This means that in Cartesian coordinates one would be able to evaluate potential contributions, say perturbations, and simply add them to the respective point's position without the need to involve the actual position itself.

Unfortunately the same is not true for the spherical coordinate system. In our case a point has coordinates (r, θ, ϕ), where the radius r is fixed for one setup so (θ, ϕ) is sufficient to define a point in space. If we apply the same example as in the Cartesian case, namely perturbing two different points with the same perturbation we will immediately see the problem. Having a perturbation of say $(\frac{\pi}{4}, \frac{\pi}{4})$ that we want to apply once to the north pole $(0, 0)$ and once to a point on the equator, say $(\frac{\pi}{2}, 0)$. The resulting points will have travelled different distances, namely $\frac{\pi}{4} \approx 0.8$ in the first and 1.05 in the second case which is a result of the non space conserving property of the spherical coordinate system. To ensure proper perturbation due to potential contributions in our system we applied the following method, in the following called north pole approach:

If we assign a middle point to a pair of particles that is subjected to a pair potential and then rotate the entire system such that the middle point is now at the north pole position we make the observation, that every perturbation of the particle positions only leads to a change in their θ components. Particles are being pushed together or apart from each other but this movement is limited to the circle on the sphere that is defined by the two points. In their original positions a movement on this arc would have resulted in a change in ϕ and θ coordinates of the point but since the circle now incorporates north and south pole due to the rotation, a position change only affects the θ coordinate of the point. Now we can apply a perturbation, obtain the resulting new positions and finally rotate the system back in its original position. With this rotation procedure we can avoid the problem of non space conservation of the spherical coordinate system.

From the resulting perturbed coordinates, individual perturbation vectors can be computed for each point that can be used to calculate the total force acting on a point during the same timestep via perturbation vector addition. The details of the approach are explained in the following. Please see also Figure 6 for an illustration.

The approach can be separated into four distinct steps:

Midpoint calculation: Given two points $v = (\theta_1, \phi_1)$, $w = (\theta_2, \phi_2)$ with $\theta_i \in [0, \pi]$ and $\phi_i \in [0, 2\pi]$ then the midpoint $p_m = (\theta_m, \phi_m)$ of v and w is

$$p_m = (\hat{\theta} + d\theta, \hat{\phi} + d\phi)$$

with $\hat{\theta} = min(\theta_1, \theta_2)$, $\hat{\phi} = min(\phi_1, \phi_2)$,

$$d\theta = \frac{1}{2} min(abs(\theta_1 - \theta_2),\ \pi\ - abs(\theta_1 - \theta_2))$$

and

$$d\phi = \frac{1}{2} min(abs(\phi_1 - \phi_2),\ 2\pi\ - abs(\phi_1 - \phi_2)).$$

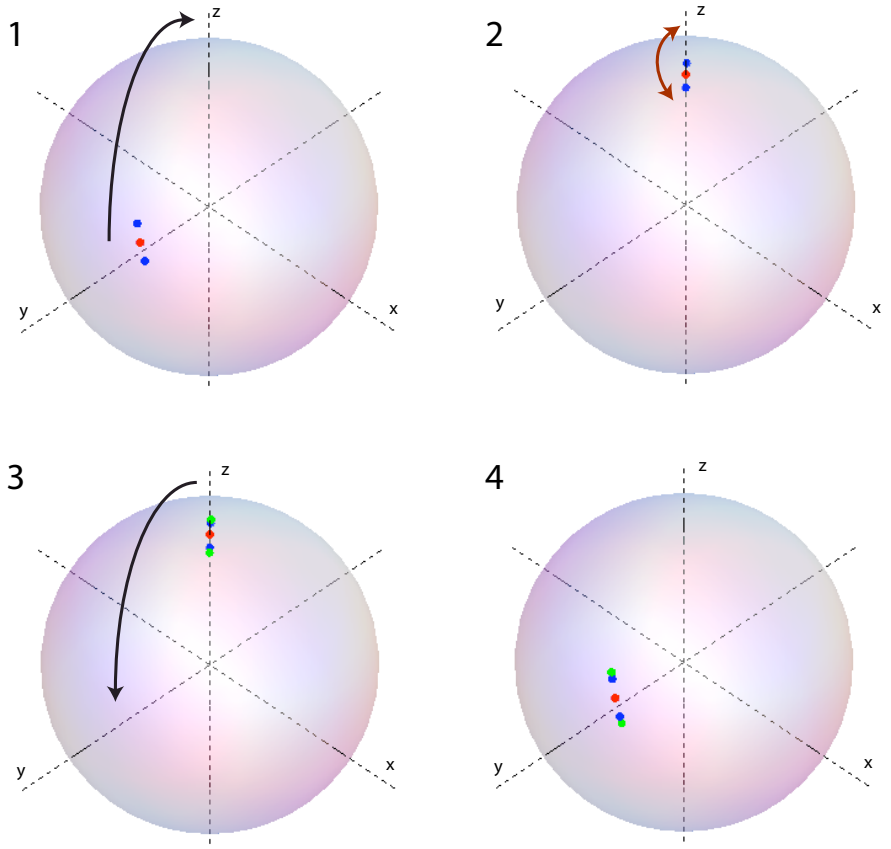

Figure 6: North pole approach for particle pair potentials. 1. For a pair of initial particle positions (blue) a midpoint (red) is computed from which a rotation matrix to the north pole is constructed for the initial points. 2. After the rotation the pair potential (dark red arrow) is evaluated on the north pole which only results in a perturbation of the θ component of the particles. 3. The perturbed points (green) are rotated back to the original position. 4. The result is a correct perturbation due to the pair potential.

This midpoint is the prerequisite for the calculation of the rotation to the north pole.

North pole rotation In order to turn the pair of points to the north pole in such a manner, that repulsion and attraction effects are only affecting their θ coordinates, we must apply a rotation that would turn the midpoint exactly to the north pole. For this reason the rotation angle is just the negative signed inclination angle θ_m of the midpoint. Since we require the rotation of the points to preserve their ϕ angles upon rotation, we take as rotation axis the unit vector in ϕ direction of the midpoint $\bar{\phi_m}$ (see also Figure 4 for an illustration) :

$$\bar{\phi_m} = (-sin\,\phi_m,\ cos\,\phi_m, 0)$$

With the rotation angle $\alpha = \theta_m$ and the rotation axis $u = \bar{\phi_m}$ we can set up the following rotation matrix:

$$R = \begin{bmatrix} cos\,\alpha + u_x^2\zeta & u_x u_y \zeta - u_z sin\,\alpha & u_x u_z \zeta + u_z sin\,\alpha \\ u_y u_x \zeta + u_z sin\,\alpha & cos\,\alpha + u_y^2\zeta & u_y u_z \zeta - u_x sin\,\alpha \\ u_z u_x \zeta - u_y sin\,\alpha & u_z u_y \zeta + u_x sin\,\alpha & cos\,\alpha + u_z^2\zeta \end{bmatrix},\ with\ \zeta = (1 - cos\,\alpha).$$

To rotate v and w we first have to converse them to Cartesian coordinates v^c and w^c via the formula given in 3.7, rotate them to the north pole obtaining v_N^c and w_N^c and transform them back to spherical coordinates to eventually obtain v_N and w_N.

Potential application Once the points have been rotated to the pole ($v_N$and w_N) the application of the potential is straight forward. The potentials used in the presented model (see Table 4) are harmonic potentials or a composition of these and only depend on the distance between two points. This distance d_{v_N,w_N} is computed as already stated in 3.7.1. The perturbation of the particle positions is now computed as follows:

Since we are in the overdamped limit, the mass of the particles can be neglected and it is the diffusion constant D that governs the magnitude of a displacement due to a potential. Since the potentials used in this system are symmetric, each particle is subjected to one half of the total force generated by the potential. This leads to the following displacements $\Delta v_N, \Delta w_N$ for the two particles:

$$\Delta i = -\frac{1}{2}\nabla V(d_{v_N,w_N})\frac{\Delta t\, D_i}{kT}$$

with $i \in (v_N, w_N)$. D_i means here the diffusion constants of the respective particle that is displaced.

To translate this displacement in means of spherical coordinates, we can use the fact, that we rotated the points to the north pole. Here all displacements manifest themselves in the θ-coordinate of the points. By using the formula for the arc length of circles we can obtain the displacement angle $\Delta\theta_i$ by dividing the displacment Δi by the radius of the sphere r:

$$\Delta\theta_i = \frac{\Delta i}{r}.$$

The new, displaced coordinates of the original points then read $v'_N = v_N + (\Delta\theta_{v_N}, 0)$ and $w'_N = w_N + (\Delta\theta_{w_N}, 0)$ respectively.

Back rotation Now the new displaced points v'_N and w'_N have to be rotated back. For this procedure the rotation matrix is the same as in the north pole rotation in the first place except for the opposite sign of the rotation angle. The coordinates of the resulting points v' and w' can now be used to compute the actual perturbation vectors that can directly be added to the initial points v and w.

$$\Delta v = v - v' \quad and \quad \Delta w = w - w'$$

These perturbation vectors are necessary since during a simulation timestep all potential contributions of a particle are computed sequentially to be added up in the end to obtain the final perturbation vector (the total force acting on that particle) that is the result of all different contributions of potentials and perturbations during that timestep.

4.1.2 Noise contributions

Concerning the noise term,

$$\sqrt{2D\Delta t}\boldsymbol{\eta}_t$$

in Cartesian two dimensional Brownian motion, the random displacement would be realized by drawing a Gaussian distributed random vector of two dimensions for η_t. However in the spherical coordinate system we are faced with the same problem of non space conservation. A Gaussian distributed random vector in θ, ϕ - space would result in different displacements depending on the point on the sphere where the displacement is appled. To overcome this problem we again use the north pole approach but in a slightly modified form. We compute the Gaussian displacment at the pole and subsequently rotate it to the point where it is meant to be applied.

Random displacement at the pole If we assume to be on the north pole a Gaussian distributed random displacement in two dimensions can be realized by first drawing randomly a direction ϕ_N, uniformly distributed in ϕ-space: $\phi_N \in [0, 2\pi]$. If we assume a walker standing on the pole, ϕ_N stands for the direction in which he decides to leave the pole in southward direction. A second, now Gaussian distributed random variable d_N is drawn that resembles the distance between -1 and 1 the walker walks in ϕ_N direction. Since the walker stands on the north pole, every change in his position towards the south is a change in the θ-coordinate of its position. We can compute this change from d_n simply by dividing it by the radius r of the sphere:

$$\theta_N = \frac{d_N}{r}$$

What we are left with is a Gaussian distributed random displacement in spherical coordinates, namely (θ_N, ϕ_N).

Adjusting the displacement by rotation For an arbitrary point p on the sphere that is meant to be randomly displaced as described above, the just computed displacement $d =(\theta_N, \phi_N)$ has to be adapted. This is achieved by rotating the displacement vector to the coordinates of p which assumes that p has been at the north pole from which the displacement started. Here the same methodology as described for potential related displacements is used. First we calculate a rotation matrix from the rotation axis, here being the unit ϕ-vector of p, and the rotation angle, here being p's θ-coordinate. Using this rotation matrix we rotate the displacement d towards the position of p resulting in the point p'.

In analogy of the potential displacement case we finally compute the point adapted displacement vector $\Delta p = p - p'$.

4.2 Parametrization and validation of the Brownian dynamics

Brownian dynamics depends on the particle interaction and the diffusion constants. Table 4 lists the particle interactions that have been used in simulations conducted here (not all potentials are active in all simulations - see Table 6 for details). These potentials are simple pair potentials of the form:

$$V(\mathbf{x}(t)) = \sum_{i=1}^{n-1} \sum_{j=i+1}^{n} V_{ij}(d_{ij})$$

whose terms only depend on inter-particle distances $d_{ij} = |\mathbf{x}_i - \mathbf{x}_j|$. The terms occurring in the present simulation model are listed in Table 4, and discussed subsequently.

Interaction pair	Description	$U(d)$
#1 - #2	Repulsion between all pairs	$\begin{cases} \frac{k}{2}(d - R_c)^2 & \text{if } d < R_c \\ 0 & \text{else} \end{cases}$
G - G	G - G repulsion	$\begin{cases} \frac{k}{2}(d - 2R_c^{\text{out}})^2 & \text{if } d < 2R_c^{\text{out}} \\ 0 & \text{else} \end{cases}$
R - R	Rhodopsin attraction potential	$\begin{cases} \frac{k}{2}(d - R_c)^2 - \alpha, & \text{if } d < R_c, \\ -\frac{\alpha k}{\beta^2}(d - R_c)^2 - \alpha, & \text{if } R_c \leq d < R_c + \frac{\beta}{2}, \\ -\frac{\alpha k}{\beta^2}[d - R_c - \beta]^2, & \text{if } R_c \leq d < R_c + \beta, \\ 0, & \text{if } d \geq R_c + \beta. \end{cases}$

Table 4: Interaction potential functions between particles. For the attraction potential α resembles the potential depth and β the distance between the potential minimum and the point when the potential is 0 again. Abbreviations used are $d = |\mathbf{x}_1 - \mathbf{x}_2|$ and $R_c = R_{c,1} + R_{c,2}$.

The most important inter-particle term is the repulsive term that prevents that particles to penetrate each other and is thus the basis for crowding and pattern formation effects on the membrane. It is described by a quadratic potential that is active if the distance d_{ij} between two particles i,j is smaller than the sum of their collision radii $R_{c,i}+R_{c,j}$ that resemble the spatial lateral extent of the particles inside the vesicle membrane. While Rhodopsin is integral to the membrane, Transducin consists of a very small anchor being in the membrane interior and a larger part situated on top of the membrane. For this reason, Transducin is assigned an inter-membrane collision radius R_c and additionally an outer-membrane collision radius R_c^{out} which is relevant for Transducin-Transducin interactions. In order to choose the force constant k, we have computed the radial distribution functions (rdf) (Eqs. (7) and (8)) of a simulation setup with only Rhodopsin (see Table 6, setup 0) composition with 25% area coverage. Since the simulation time step depends on the potential used, these rdfs were calculated without a dynamical simulation and instead using the Monte Carlo algorithm described in appendix A4. The result shown in Fig. 7 suggests that a force constant of 0.25 is sufficient to maintain spatial exclusion of the proteins. Hence, $k = 0.25$ was used for all repulsion potential terms.

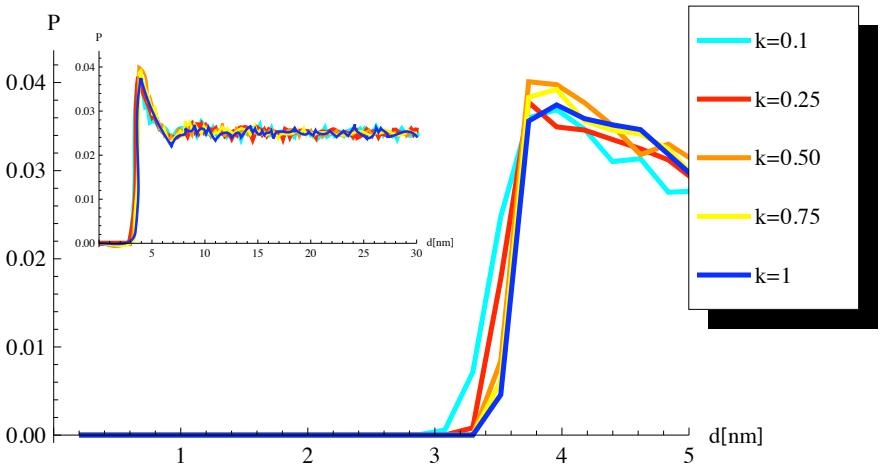

Figure 7: Radial distribution function of Rhodopsin-filled membranes (setup 0) with different force constants for particle repulsion.

In order to test the effect of Rhodopsin pattern formation on the phototransduction module, an attractive potential between Rhodopsins was considered as well. Its functional form is given in Table 4. It consists of the repulsive quadratic potential described above, down shifted by the depth of the potential α, plus two additional terms $g(d)$ and $h(d)$. Together these functions describe a potential which is repulsive for particle distances between 0 and the sum of the particle distances $R_c = (R_{c,1} + R_{c,2})$, has a minimum at this point R_c of value α ($U(r_0) = \alpha$) and rises again to 0 over a length of β ($U(d) = 0$, if $d > \beta$). This potential is up to now only used for theoretical studies of particle crowind effects on the vesicle (see Section 7.1).

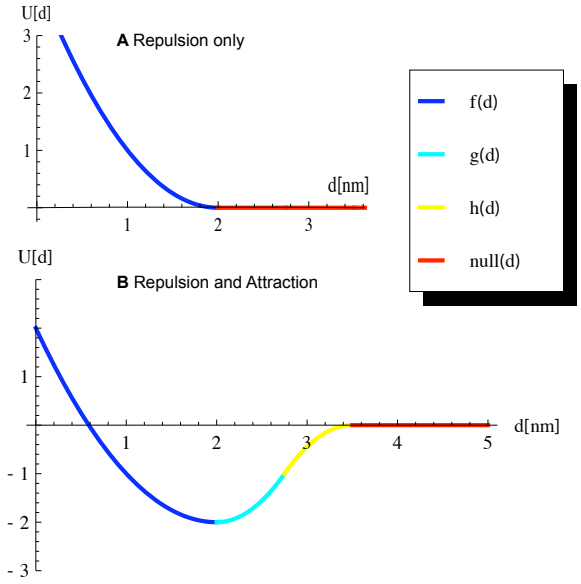

Figure 8: The potential functions used in the simulator. A purely repulsive potential, B repulsive-attractive potential used in simulation setup B.

For a given definition of the potential, the Brownian dynamics simulation time step Δt must be adjusted. This is because the time discretization (4) is a local linearization of the nonlinear potential, which is only a good approximation when the time step is small enough compared to the curvature of the potential. Thus, stiffer potentials require shorter time steps. Here, we chose an initial value for the diffusion constant of $D = 3D_{macro}$ and adjusted the time step such that the Brownian dynamics simulation yielded the same stationary behavior as the Monte Carlo algorithm described in Appendix A4. Fig. 9 shows a comparison of the Rhodopsin-Rhodopsin radial distribution functions (see Eq. (7) and (8)) calculated with the Monte Carlo algorithm, and the Brownian dynamics discretization using time step $\Delta t = 7.5$ ns, which was used henceforth. Significantly larger time steps resulted not only in differences of the radial distribution function, but also in an undesirable dynamical behavior, where particles were observed to cause clashes, and the large forces caused them to make large steps that often caused other clashes immediately. Using time steps of 7.5 ns or less is thus essential for a stable simulation given the present inter-particle potential settings.

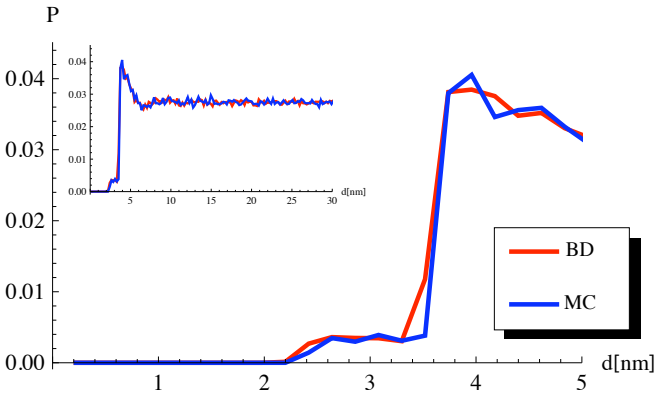

Figure 9: Validation of the numerical correctness of the simulation. The radial distribution function of Rhodopsin in a pure Rhodopsin simulation is calculated with Monte Carlo method (blue line, see Appendix for description of the method) and Brownian dynamics simulation using a time step Δt =7.5 ns (red line, see Sec. 3.2).

Finally, the microscopic diffusion constants needed to be adjusted such that the resulting macroscopic diffusion constants matched the experimentally measured diffusion constants of R and G. Fig. 10 shows the mean square deviations for a simulation containing both R and G (simulation setup A, see Table 6) of 10 μs length. The differences between microscopic and macroscopic diffusion are clearly visible due to the linear fits on short and long timescales. The R-G mixture is apparently dilute enough such that the difference between microscopic and macroscopic diffusion constants is small. Setting $D = 0.85$ and 1.55 $\mu m^2 s^{-1}$ for R and G, respectively, yielded macroscopic diffusion constants similar to the experimental values of $D_{obs} =$ 0.7 and 1.3 $\mu m^2 s^{-1}$ [43].

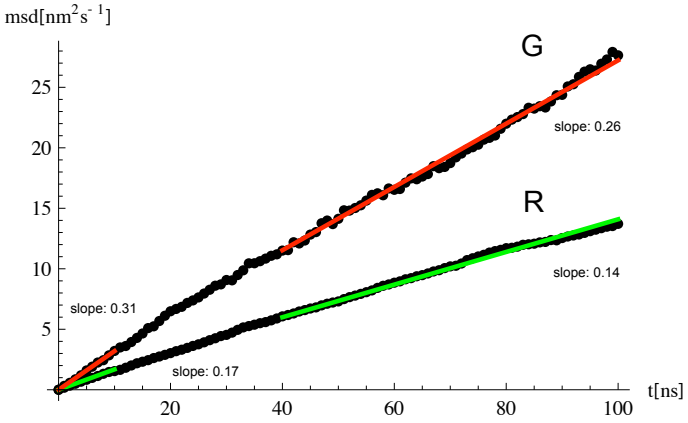

Figure 10: Microscopic versus macroscopic diffusion constants for Rhodopsin (R) and Transducin (G) on a disc membrane: The mean square displacements (msd) $msd = \langle(\mathbf{x}(0) - \mathbf{x}(t))^2\rangle$ of R (lower curve / green fit) and G (upper curve / red fit) were estimated from a 1 μs simulation trajectory of a pure R/G mixture on a vesicle. The msd's have a slope of $2D$ for short times and then converge to lines with slope $2D_{\text{obs}}$ for long times. D was adjusted so as to obtain the experimentally measured diffusion constants as value as D_{obs} (see text).

4.3 Particle reactions

The reactions in the present simulation setups are mainly realized *via* unimolecular reactions. This is due to the fact that GTP and GDP are not built into the simulation explicitly but the rates which depend on availability of GDP and GTP from the solution are set depending on their concentration (in our setup, [GDP] = 1 and [GTP] = 3000). This assumes that GDP and GTP are homogeneously distributed at all times, which is a good approximation as their diffusivity is about a factor of 100 greater than the diffusivities of R and G. Thus, the spatial distributions of GDP and GTP can be assumed to be averaged out on the timescales relevant to the on-membrane events.

An overview over all reactions involved gives the following network:

$$MetaI \underset{k_{-1}}{\overset{k_1}{\rightleftharpoons}} MetaII(= R^*)$$

$$G_{GDP} + R^* \underset{k_{-2}}{\overset{k_2}{\rightleftharpoons}} G_{GDP}R \underset{k_{-3}(GDP)}{\overset{k_3(GDP)}{\rightleftharpoons}} G_0R^* \underset{k_{-4}(GTP)}{\overset{k_4(GTP)}{\rightleftharpoons}} G_{GTP}R^* \underset{k_{-5}}{\overset{k_5}{\rightleftharpoons}} G_{GTP} + R^*$$

$$G_{GTP} \underset{k_{-6}}{\overset{k_6}{\rightleftharpoons}} G_{GTP}(SOL)$$

The reaction rates are taken from [27] see also Section 2.

Table 5 gives an overview over all possible reactions and their rates and probabilities.

Symbol	k	k_a	p
k_1	$28\ s^{-1}$	..	$2.1\ \times 10^{-7}$
k_{-1}	$15\ s^{-1}$	..	$2.125\ \times 10^{-7}$
k_2	$0.53\ \frac{\mu m^2}{s}$	$20710.5\ s^{-1}$	$1.553\ \times 10^{-4}$
k_{-2}	$283\ s^{-1}$	..	$2.123\ \times 10^{-6}$
$k_3(GDP)$	$607.5\ s^{-1}$	..	$4.556\ \times 10^{-6}$
$k_{-3}(GDP)$	$2.22\ s^{-1} \times [GDP]$	$2.22\ s^{-1}$	$1.665\ \times 10^{-8}$
$k_4(GTP)$	$2.6\ s^{-1} \times [GDP]$	$7800\ s^{-1}$	$5.85\ \times 10^{-5}$
$k_{-4}(GTP)$	$0\ s^{-1}$	..	0
k_5	$48600\ s^{-1}$	..	$3.644\ \times 10^{-4}$
k_{-5}	$0\ s^{-1}$	..	0
k_6	$10000\ s^{-1}$	..	$7.5\ \times 10^{-5}$
k_{-6}	$0\ s^{-1}$	..	0

Table 5: Reactions between particles involved in the current simulation, the rate constants k of the activation step, the microscopic rate constants k_a (if different from k) and the probability that such a reaction happens on base of a timestep of $\Delta t = 7.5$ ns.

4.4 Initial conditions and parameters of the simulation

In this section all initial conditions and parameters for our simulations are summarized:

Global parameters The global parameters governing our simulation is the temperature which has been $22°C$ in the experiments and the timestep of $7.5\,ns$ that we use for all of our simulations.

Vesicle size We simulate a disc vesicle of radius $70\,nm$ which makes $\frac{1}{10}$ of the area, Heck and Hofmann assumed the standard vesicle to have in their experiments. We decided to simulate this fraction for computational cost issues since one $100\,ms$ trajectory of this small vesicle already takes two weeks for computation.

Particle configuration Based on the experiments of Heck and Hofmann we took six setups of different G-protein concentration around the physiological concentra-

tion of G40. See Table 6 for an overview.

	G10	G20	G30	G40	G50	G60
R	1538	1538	1538	1538	1538	1538
MetaII (R*)	1	1	1	1	1	1
G	21	40	88	156	228	335

Table 6: Simulation parameters that are either global or local parameters that vary in different simulations. The other particle species available in the simulation are not present in the initial setups but can be created during the simulation. Setup G40 resembles G-protein concentration under physiological conditions.

Each setup starts with the physiological number of 1539 Rhodopsin molecules from which one is in its active form. In the experiment at time $t = 0$ the light flash is applied to the system which induces some Rhodopsin molecules to immediately change its conformation to a pre-active state MetaI which, after a certain time, changes to the active state MetaII. The average waiting time for such an event to happen is $35.7\,ms$. Concerning our maximal trajectory length of $100\,ms$ we would end up simulating nothing interesting for around $\frac{1}{3}$ of our time until a MetaII form of Rhodopsin appears that can activate G-proteins and can induce interesting processes to happen.

For this reason we discard this initial delay of the dynamics for our simulation and start directly with MetaII at time $t = 0$. The next paragraph explains how the effect of the MetaI - MetaII delay can be applied to the finished trajectories after the simulation without the need to have it included in the dynamics.

Meta II effect The reaction from MetaI to MetaII is a unimolecular decay reaction with rate $28\,s^{-1}$. When we start our simulation with a MetaII instead of a MetaI but leave all other reactions, e.g. the back reaction from MetaII to MetaI, in the system, the only thing that differs in our simulated trajectories compared to real ones is a certain delay that is not present in our simulations caused by the slowly increasing probability that the first reaction from MetaI to MetaII has happened already.

However this delay can be specified exactly to be:

$$p(t) = 1 - exp[-t\,k]$$

which means the probability, that the reaction with rate k has happened from time $t_0 = 0$ up to time t , is $p(t)$. The shape of $p(t)$ is illustrated in Figure 11. After $100\,ms$ $p(t)$ is $> 90\%$.

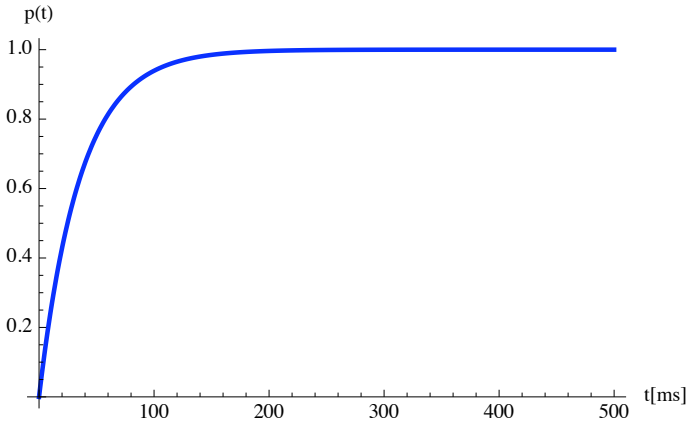

Figure 11: Probability that the reaction from MetaI to MetaII has happened already from time $t_0 = 0$ to time t.

We can obtain a recovery of the real dynamics from our simulated one where the first reaction from MetaI to MetaII is neglected by weighting the simulation results by $p(t)$.

Equilibration of the start structure All simulations start from an initial structure where all particle species present at time $t = 0$ are uniformly distributed on the simulated vesicle surface. However, since our particles have a certain extension in space, this random structure is likely to produce very unfavorable overlaps between particles. A simulation start from this conformation would get the system to explode within few steps since large repulsion forces between the overlapping particles would cause them to be diverted very fiercely which is very likely to produce other overlaps somewhere else starting a chain reaction.

To avoid this behavior the first uniform distributed random conformation has to be equilibrated first. We do this by applying the Monte Carlo (MC) algorithm described in 3.6 for 3000 steps at a timestep $\Delta t = 100$ns. Figure 12 depicts the initial random structure and the result of the minimization. Furthermore the trajectory of the potential energy of the structure is plotted which shows a very high initial energy due to multiple particle-particle overlaps. From this high maximum, the energy drops quite fast to fluctuate after about 1000 steps around a minimum energy. Having reached a plateau at the minimum means that the structure is equilibrated and major clashes between particles have been removed.

Due to the large timestep used during minimization, the random displacements of particles during the MC-algorithm still produce minor clashes between particles which leads to a fluctuation around the minimal energy in the trajectory of the potential energy. However these minor overlaps can be handeled by the Brownian dynamics simulator and disappear there within few hundreds of timesteps.

Particle parameters and diffusion constants Please see Table 3 for an overview over all particle species used in the simulation and their respective parameters in-

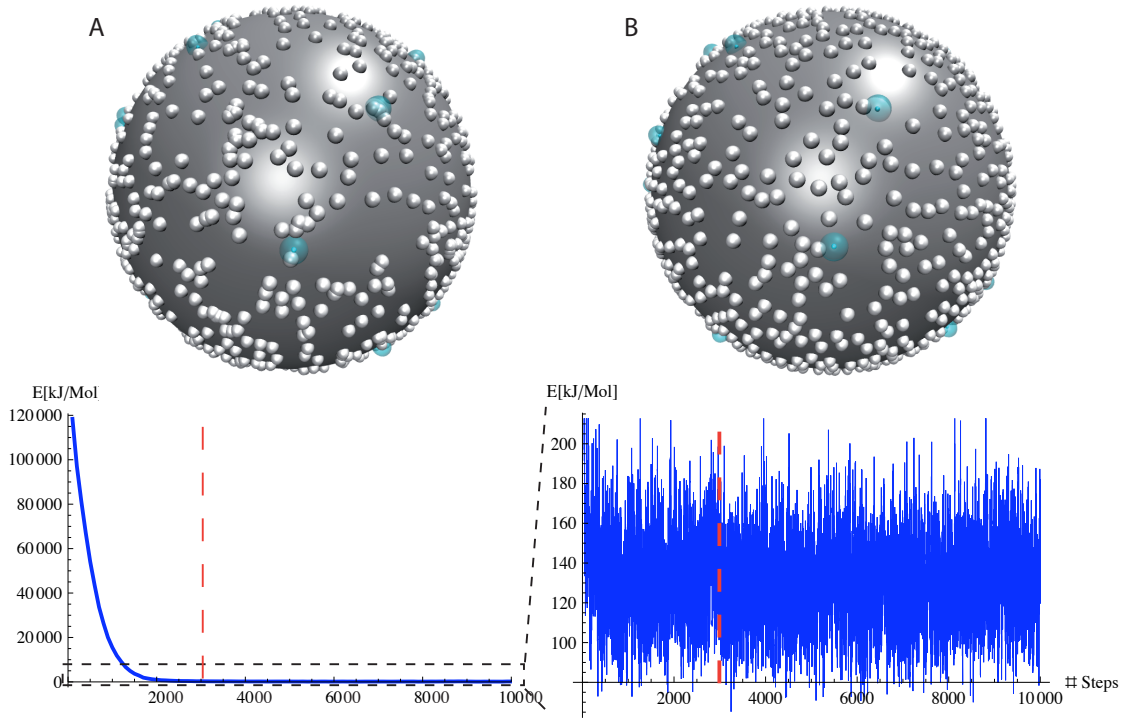

Figure 12: Minimization of initial structures using Monte Carlo (MC) sampling for 3000 steps at a timestep of $\Delta t = 100ns$: Generating uniform distributed random structures on a sphere leads to multiple clashes between particles (A). These clashes have to be removed first before the conformation can be used as initial conformation in the Brownian dynamics (BD) simulation. Applying the MC-algorithm penalizes unfavorable clashes that lead to a high potential energy. In consequence the potential energy is minimized and reaches a minimal plateau (lower left figure). The generation of minor particle-particle overlaps in each timestep leads to a fluctuation around the minimal energy (lower right figure). After 3000 steps the simulation is converged and all major clashes between particles have been removed (B). This structure can now be used as input for the BD simulator.

cluding their microscopic and macroscopic diffusion constants.

Reaction Rates Table 5 gives an overview over all reactions used in the simulation together with their microscopic and macroscopic rates and their probability to happen during our timestep of $\Delta t = 7.5$ ns in the Brownian dynamics simulation.

4.5 Efficient neighbor calculation

In particle dynamics simulations the task of calculating neighbors of particles occurs very frequently. All particle-particle interactions as repulsions or reactions are based on the spacial proximity of particles and involves in consequence the calculation of inter particle distances as a prerequisite.

The naive approach to this problem would simply be the caluculation of all pairwise particle distances in the system for each time step. However this approach would have run time complexity of $O(n^2)$ which would dominate our whole algorithm which otherwise only consists of parts of linear complexity $O(n)$. In the following, methods are described that allow neighbor searching in linear complexity as well.

4.5.1 Lattice approach for neighbor calculation

For most purposes, at least for all occuring in our simulation, effects involving particle distances are limited on a certain range. E. g. reactions only occur between particles if they come closer to each other than a certain interaction distance r_i. The same applies for particle repulsion where two particles A, B start to repell each other if they have a smaller distance than the sum of their radii $r_A + r_B$. In such cases it makes sense only to scan the direct neighborhood of a particle for possible interaction partners than to check every particle in the system for possible proximity.

This can be achieved by setting up a grid in particle space with a box spacing r_{box} that is the maximum over all interaction distances and particle radii in the system: $r_{box} = 2 \times max(r_{interaction_i}, \forall r_{particle_j})$. If we now look for the possible interaction partners for a certain particle p and know it's grid box, we only have to check all particles in the first layer of boxes around it for potential candiates. Per construction of the grid, all particles not within these boxes are too far away from p for any interaction.

In the worst case, using a grid in this way will not perform better than $O(n^2)$. In such a scenario all particles would be placed in the same box which would still require the calculation and comparison of all particle-particle distances. Yet this is a very unlikely case in real world examples Especially in our simulation all particles are more or less homogeneously distributed in space and have shapes and interaction radii that allow for a very fine-meshed grid. Here, in each neighborhood analysis, an average number of particles have to be checked that is much smaller than the total number of particles in the system. This would lead in our case to a linear average complexity of $O(n)$.

4.5.2 Lattice on a sphere

The setup of a grid as described in the previous subsection is straight forward in Cartesian coordinates but has to be handled carefully in spherical coordinates. As depicted in Figure 13, simply drawing a grid over θ-ϕ-space (A i) results on the sphere (A ii) in grid boxes of different sizes and even worse differently distorted shapes.

To construct a grid of the desired properties, we first have to assess in which way the space is distorted by the coordinate transformation from spherical to Cartesian coordinates. Starting from the transformation rules as already given in Paragraph 3.7 we evaluate the Jacobian matrix

$$J(r,\theta,\phi) = \begin{bmatrix} \frac{\partial x}{\partial r} & \frac{\partial x}{\partial \theta} & \frac{\partial x}{\partial \phi} \\ \frac{\partial y}{\partial r} & \frac{\partial y}{\partial \theta} & \frac{\partial y}{\partial \phi} \\ \frac{\partial z}{\partial r} & \frac{\partial z}{\partial \theta} & \frac{\partial z}{\partial \phi} \end{bmatrix} = \begin{bmatrix} sin\theta\, cos\phi & r\, cos\theta\, cos\phi & -r\, sin\theta\, sin\phi \\ sin\theta\, sin\phi & r\, cos\theta\, sin\phi & r\, sin\theta\, cos\phi \\ cos\theta & -r\, sin\theta\, cos\phi & 0 \end{bmatrix}$$

and calculate its determinant

$$Det(J) = r^2\, sin\theta.$$

We see that the determinant is independent of the ϕ-angle which means that the space transformation from spherical to Cartesian coordinates is also independent of ϕ. The most important dependence lies in the θ-angle. Here the area of a surface element changes with the sinus of the θ-angle at its position which means, given the range of θ being in $[0,\pi]$, that the area is preserved at the equator ($\theta = \frac{\pi}{2}$) and is compressed to 0 at the poles ($\theta = 0$; $\theta = \pi$). With this observation we can setup a grid on a spherical surface whith near uniform area elements. However the number of these grid elements will vary, depending on the position on the sphere.

In more detail the observations above result in a grid that has a constant number of subdivisions on the θ axis, in the following called θ-stripes but the number of subdivision in each stripe in the ϕ dimension varies according to the θ value of the stripe. More specificly, following from the spatial dependence of the coordinate transformation upon the respective θ-value, the number of subdivisions in each θ-stripe is the ceiling of the desired maximal number of subdivision at the equator $N_{\phi max}$ weighted by the sinus of the θ-value of the given stripe:

$$N_\phi(\theta_i) = \lceil N_{\phi max}\, sin\, \theta_i \rceil.$$

where θ_i is the θ-value of stripe i, being its midpoint. There is however one exception to this rule: The first and the last θ-stripes contain per definition only one box because they contain the pole regions, the areas with infinite area distortion upon coordinate transformation. Any subdivision in these areas would fail.

The result of this calculation is illustrated in the following example: Say that we want a box size of $\frac{\pi}{7} \times \frac{\pi}{7}$. We first compute the number of θ-stripes and their midpoints: If we equally subdivide the range of $\theta \in [0,\pi]$ in parts of length $\frac{\pi}{7}$, we obtain 7 stripes with midpoints $\frac{i}{14}\pi$, $i \in \{1,3,5,7,9,11,13\}$. See also Figure 14

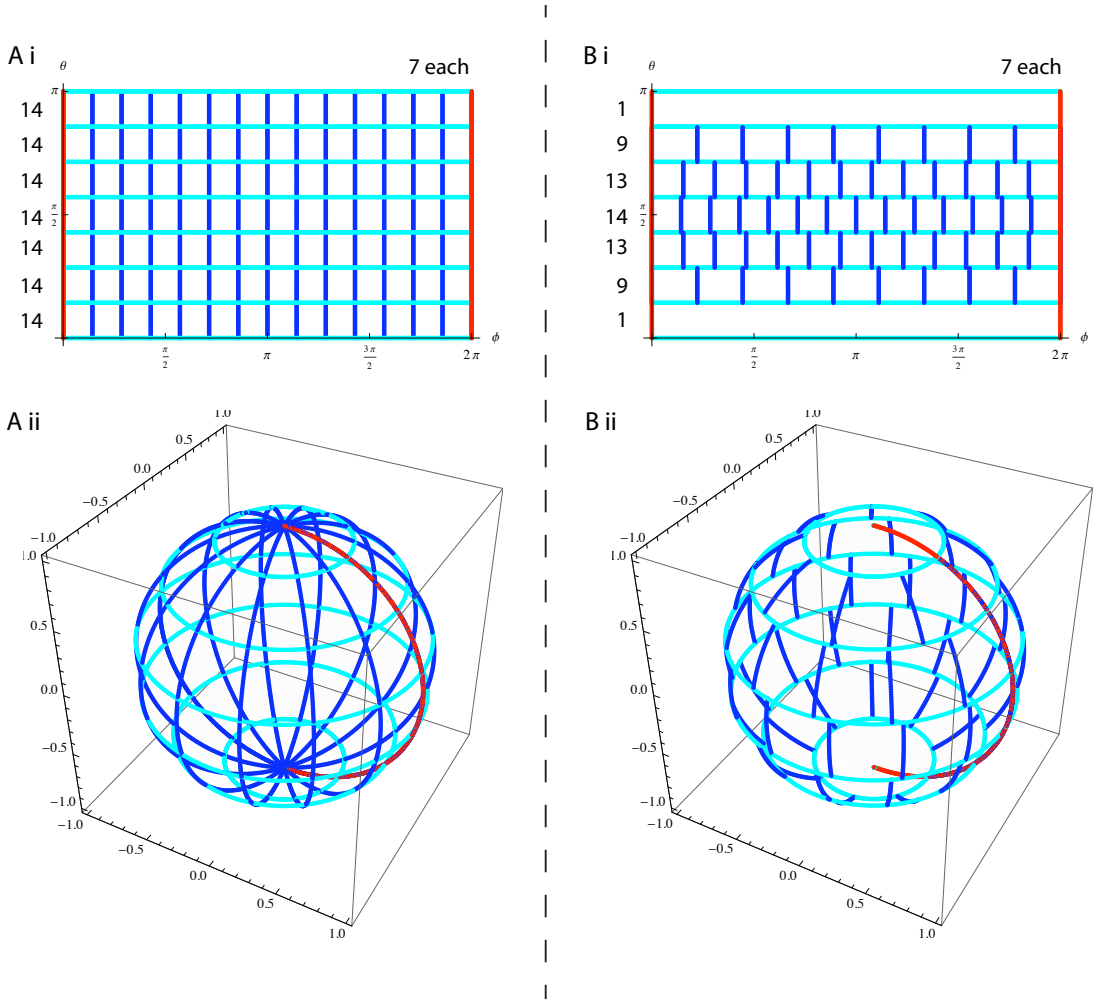

Figure 13: Illustration of the special properties for constructing a lattice in spherical coordinates. The setup of a uniformly spaced grid in (θ, ϕ)-space (A i) results in distorted and unhomogeneous grid boxes in Cartesian space (A ii). The desired properties of homogeneous grid boxes in Cartesian space can be achieved by still subdividing θ uniformly into θ-stripes, but subdividing ϕ depending on the respective θ-value of the stripe (B i). Remark that the poles are covered by one box only because here the space distortion becomes infinitely high. The result is projected to Cartesian coordinates reveals the success of the approach.

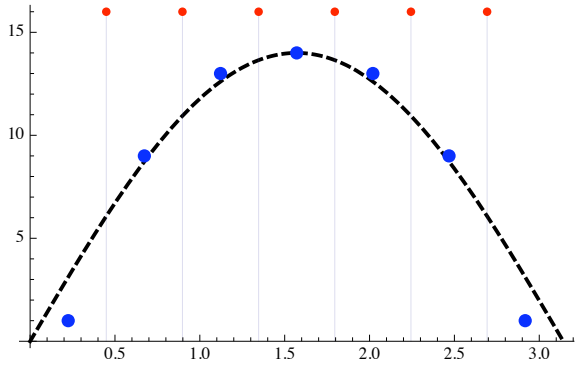

Figure 14: Illustration for the computation of the number of subdivisions in a θ-stripe. The red pointed needles resemble the borders of θ-stripes. The dashed line depicts $N_{\phi max} \times sin\,\theta$ which is only evaluated and rounded to the ceiling at the midpoints (blue) of the respective θ-stripes. The first and the last stripe, incorporating the north and the south pole of the sphere are covered by one box only.

where the stripes and their midpoints are depicted. In the next step we compute the number of subdivisions for each θ-stripe: $N_{\phi max}$ is the number of boxes at the equator which is the number of subdivisions of length $\frac{\pi}{7}$ in which we can split the range of $\phi \in [0, 2\pi]$. This evaluates to 14 subdivisions. Using the formula above we compute $N_\phi(\theta_i)$ for each stripe, resulting in $\{1, 9, 13, 14, 13, 9, 1\}$.

With this information we can setup a grid that has the desired properties of equally sized boxes. See also Figure 13for an illustration of the constructed grid from the example.

4.5.3 Neighborhood assignment in a spherical lattice

As outlined before, the setup of the lattice is only a prerequisite for the actual task: The computation of the neighborhood of a current box within a grid. Again this appears to be a special problem in spherical coordinates compared to a grid in Cartesian coordinates. See Figure 15 for an illustration.

Following the setup of the grid as described above we end up with a number of θ-stripes that contain different numbers of boxes. Say we want to compute the neighborhood of point p, having index (i, j) in the grid. From this index we can compute the neighboring indices in that particular θ-stripe S_θ of p, being $(i-1, j)$ and $(i+1, j)$.

To obtain the neighboring boxes in the θ-stripes to the left $S_{\theta-1}$ and to the right $S_{\theta+1}$ we do the following: We add and substract 1.5 times the ϕ-box length in S_θ to and from the midpoint m_p of the grid box of p (orange arrows in Figure 15). The resulting points m_{p-} and m_{p+} points lie on the outer boundary of the neighboring boxes in S_θ. From each of these points we now go in θ-direction for $\pm$ the box length in θ (red arrows in Figure 15).

We now have generated four points $m_{p\pm\pm}$ around the initial grid box that each can be assigned to a grid box themselves. $m_{p-+}$and m_{p--} lie in the θ-stripe $S_{\theta-}$

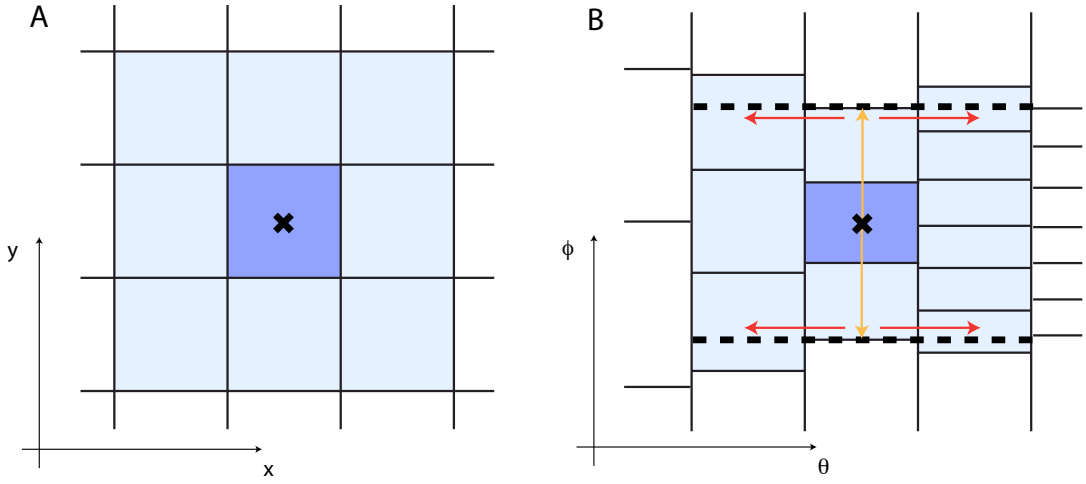

Figure 15: Illustration of the neighborhood search in a spherical lattice (B) compared to a grid in Cartesian coordinates (A). In the spherical case additional boxes have to be taken into account for the neighborhood because of the space distortion during the transformation from spherical to Cartesian coordinates. Note the equidistant subdivisions in θ in contrast to the changing number of boxes in each θ-stripe. The orange and red arrows depict the method of midpoint extension to find the neighborhood in spherical case.

to the left of S_θ, and m_{p++} and m_{p+-} lie in the stripe to the right $S_{\theta+}$. We now define all boxes as neighboring boxes of p that lie between these four points in $S_{\theta-}$ and $S_{\theta+}$. This method may lead to a neighborhood that is sometimes larger than necessary but it will in no case miss a potential neighbor.

4.6 Runtime of the algorithm

Fig. 16 shows the CPU time required for a single time step in order to illustrate the linear scaling and the efficiency of the particle simulator. For this, vesicles of different sizes containing differently many simulation particles (but keeping the concentrations of R and G constant) were simulated. The tests were run on single cores of quadcore Intel Xeon CPU E5345 with 2.33 GHz. The scaling of the CPU time with the number of particles is linear up to ∼15,000, the slightly superlinear behavior after that is probably due to memory effects. This linearity is due to an efficient neighbor look-up scheme used in each simulation iteration before inter-particle distances are calculated (see Appendix for details), without which the scaling would be quadratic. For the given implementation, one iteration of the simulation setup containing ∼1,500 particles takes ∼64 ms, considering the simulation time step of 7.5 ns this means that trajectories of 10 ms can be simulated within about one wall-clock day on a single CPU core. Note that much of this efficiency is due to the fact that only membrane proteins are simulated here. Soluble molecules diffuse about a factor of 100 faster and would thus require a simulation time step about

100 times smaller, also slowing down the simulations effectively by a factor of 100.

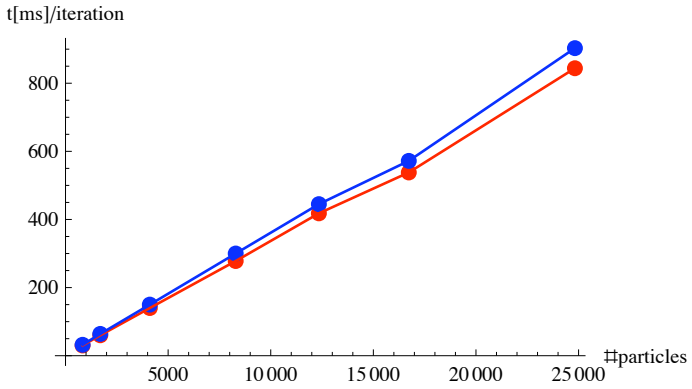

Figure 16: CPU time required (using single standard CPU cores) for one iteration of the simulated systems including Brownian dynamics and reactions, depending on the number of particles simulated. The red curve indicates the particle Simulation without reactions, the blue one had reactions included.

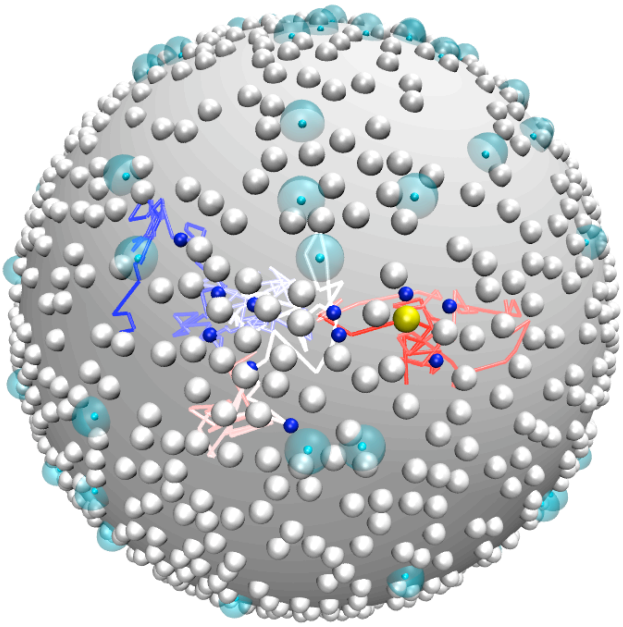

Figure 17: An example trajectory of our system with accellerated reaction rates, simulated for 1.5 ms. The following particle species are visible: Inactive Rhodospin (white), active Rhodopsin MetaII (yellow) and inactive G-protein (cyan) that is depicted with its membrane internal radius (small, opaque) and its radius on top of the membrane (large, transparent). The trajectory of MetaII is illustrated in colors ranging from red over white to blue, indicating its time course during the simulation time. Activated G-proteins, once activated, dissolve very quickly from the membrane. The spots where such dissociation events from activated G-proteins happened are marked with small blue dots.

5 Results

In the following section the results of the modeling and simulation work are presented. Unfortunately the ordinary visual inspection of simulation trajectories is no more applicable on trajectories of length of at least 3×10^7 steps and is furthermore not quite objective. However Figure 17 is presented the reader to get an impression on how the generated trajectories actually look like.

5.1 Purely diffusion-limited output rate

A theoretical upper bound to the $G*$ production rate upon single photon activation was estimated to be 7000 s^{-1} in [36] based on simple arguments using two-dimensional reaction-diffusion kinetics and estimations of the reaction parameters. Here we can explicitly calculate this bound by taking the following limits (see Table 5): (i) GTP was considered to be highly concentrated such that $\mathrm{R^*G_0} \xrightarrow{+GTP} \mathrm{R^*G}_{GTP}$

occurs instantaneously, (ii) GDP was considered in zero concentration such that the unproductive back-reaction $R^*G_{GDP} \xleftarrow{+GDP} R^*G_0$ occurs never, (iii) all physico-chemical dissociation events occur instantly, i.e. k_1, k_2 and k_3 are ∞. In this limit, the $G*$ production rate is only limited by diffusion initially, but will asymptotically decrease to zero as G is depleted on the membrane. Thus, the maximum rate is obtained at short times. Fig. 18 shows the cumulative $G*$ production and the linear fit indicates an estimate of the maximum rate of $\sim$8455 s^{-1}. Despite the simplicity of the arguments in [36], the estimate given there is surprisingly accurate. However, it needs to be noted that both the estimates in [36] and here are only valid bounds if all particles are in fact diffusing freely and isotropically with the diffusion constants given in [43]. Any type of anomalous diffusion due to e.g. formation of Rhodopsin dimers or oligomers would reduce this upper bound.

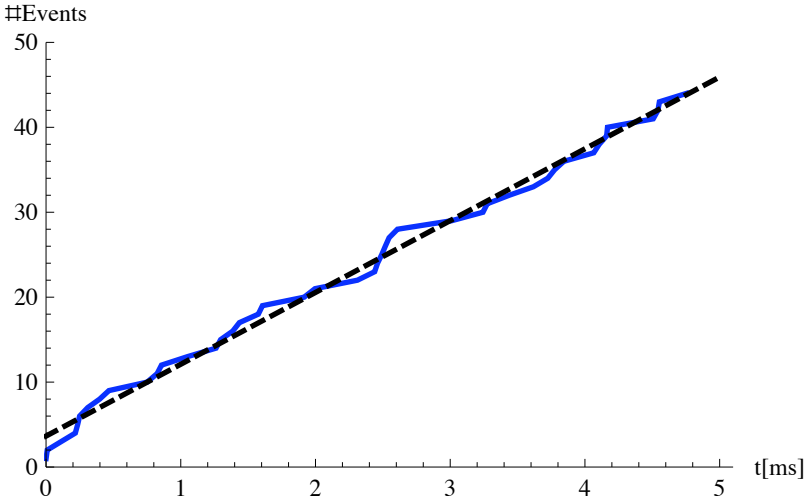

Figure 18: Upper bound (diffusion-limited) of the cumulative $G*$ production (blue). The dashed black line shows a linear fit indicating a rate of 8455 s^{-1}.

5.2 Simulation of the experimental setup

To gather enough data for reliable statistics, 16 simulations were run for 100 ms for each G-protein configuration (see Table 1), using the simulation setup and initial conditions presented in 4.4. In total 96 simulations were performed, each taking on average two weeks for completion which resulted in the investment of 1344 computaton days for this study.

5.2.1 Features of individual trajectories

Figure 20 depicts the cumulative number of each reaction event that happened during the simulation of three chosen trajectories from the G10 setup. See Figure 19 for an explanation of the color coding of trajectory figures.

On the time resolution of milli seconds only the rare reaction events are visible and can be distinguished from others. Especially reaction events that happen in a

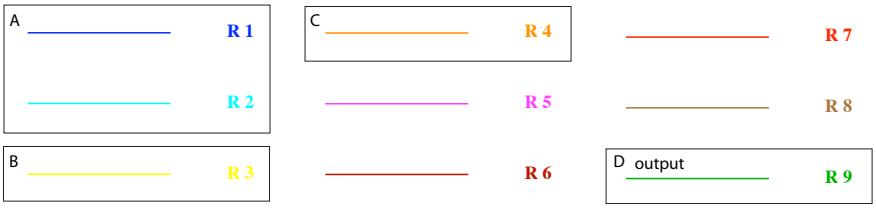

Figure 19: Color coding of reaction events. The predominant reactions, visible in plots of trajectories are marked with a box. A: R1 and R2 mark the reactions between the MetaI and MetaII. These are quite rare events but have a high impact since a reaction from MetaII to MetaI (k2) prevents all other reactons from happening. B: The complex formation reaction between R* and G. C: The dissociation reaction of the R*G complex. D: Due to their high reaction rate, reactions 5, 6, 7, 8 and 9 folllow each other in such small time intervals that they all disappear behind the plot of the last reaction 9 which depicts the dissociation reaction of G* from the membrane, the desired output of the simulation.

short time subsequently to each other may be hidden behind the last reaction in that queue. Because of this effect, reactions 5 to 8 are hidden behind the time course of reaction 9 in the presented figures.

However the time courses that are visible show the important features of the trajectories: The most important one is the course of events of G* membrane dissociations, depicted in green color which states the experimentally measured output. The two other curves show the number of complex formation events between R* and G (yellow, above the green one) and their dissociation (orange, below the green one).

There are times, where all three of these curves form a plateau. This is especially the case in trajectories A and B and happenes after a MetaII to MetaI reaction event took place (depicted as cyan curves). Until a backward reaction happens (blue curves) all other reactions are blocked since MetaI is not capable of G-protein activation. Such blocking periods are illustrated in the figures by an asterisk.

The diffusive finding of R* and G and all subsequent reactions that finally end up by a dissociation event of an activated G-protein are stochastic processes that demand averaging over multiple realizations. Blocking periods of the receptor and an increasing G-protein depletion over time due to their activation and dissociation increase the variability of the trajectories additionally. In this sense, the next section deals with the analysis of an ensemble of trajectories.

5.2.2 Statistics for one G-protein setup

To compare our simulation results with expermental data we have to average over multiple realizations. Figure 21 illustrates the mean and the standard error over 16 realizations of the G40 setup which resembles physiological conditions. It is remarkable, that despite the stochasticity of the process and receptor blocking events

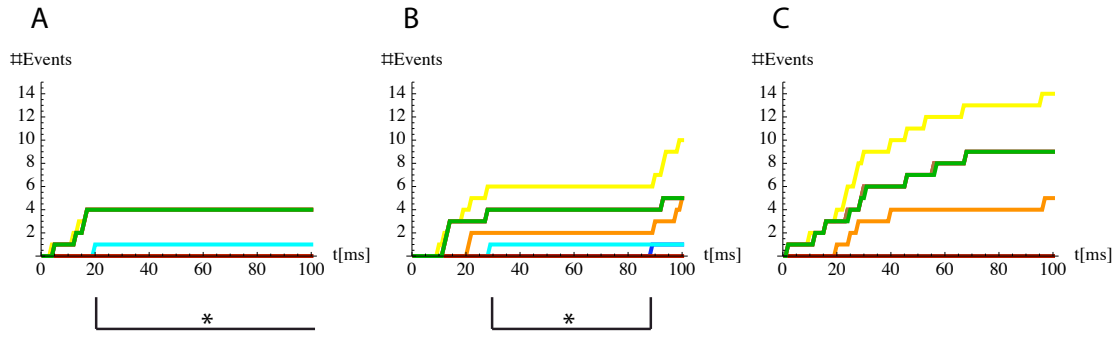

Figure 20: Cumulative number of events of three realizations of setup G10. Please see Figure 19 for the color coding. It stands out, that trajectories A and B have a much smaller active G-protein output (green curve) than trajectory C. The reason for this is an occurred back reaction from the active, G-protein activation capable MetaII form of Rhodopsin, to the passive MetaI form. Events of this form are colored in cyan. During the absence of MetaII no further reactions in the signalling pathway can occur. While in A the MetaII never comes back again, it reappears in B at 90ms leading to further production of active G-protein. The time periods of MetaII absense are marked with an asterisk (*).

the number of G* dissociation rises quite uniformly. We will elaborate on this observation later in section 6.

Although we have now the average number of G* dissociation events we can not compare these numbers to the experimental data yet. The next section will outline the reasons and describe the results of making them comparable.

5.2.3 Postprocessing of trajectories

When we average all realizations of a given setup and plot their number of G* dissociation events against the experimental data, we get the following picture (see Figure 22 A) which doesn' t look very promising.

The reason is that we underestimate our results and have to reweight them first. Heck and Hofmann published in their experimental setup that every flash of light activated $5.7\,R^*\mu m^{-2}$ on their disc vesicle membranes. Our simulated vesicles have a radius of $0.07\mu m$ which results in a surface area of $0.061\mu m^2$. In this respect we would have $0.35\,R^*$ per vesicle. However every simulated trajectory started with one R^* instead of only every third. In consequence we have to reweight our trajectories by a factor of $\frac{1}{0.35}$. The result can be seen in Figure 22 B. No it looks much more comparable to the experimental data.

Yet we still have to include the effect that all trajectories started with Rhodopsin in the active MetaII form instead of MetaI. As already outlined in Paragraph 4.4 the effect can be included by an additional reweighting of the simulated trajectories according to the probability that the reaction from MetaI to MetaII has already happened from time $t = 0$ to time t. Figure 22 C depicts the result of this final

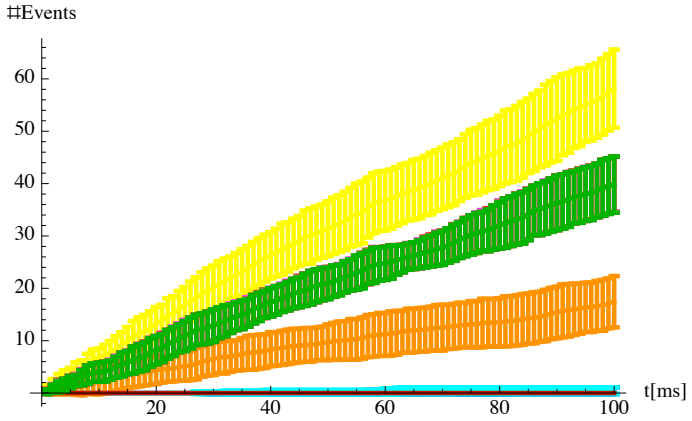

Figure 21: Average over the cumulative number of events of 16 realizations of the G40 setup which resembles physiological conditions. Please see Figure 19 for the color coding.

weighting.

The last step reveals remarkable agreements between our simulated trajectories, the experimental data and the fitted ODE model, at least for setup G10, G20 and G30. The average trajectories of G40, G50 and G60 seem to fit well in the first part until about 50ms but then start to underestimate the experimental values. A remarkable fact is also that the average trajectories of G10 and G20 seem to follow the experimental and ODE descriptions almost perfectly until they reach a certain number of dissociated G* and continue from this point on with a smaller slope. Please see Section 5.3 where this detail is analysed furter.

5.2.4 Statistics for all G-protein setups and their comparison to experimental data

After the two steps of reweighting we can compare our simulation results to the experimental data and the ODE model from Heck and Hofmann. Figure 23 shows the average cumulative numbers of reaction events together with their standard deviation of all reactions present in the simulation. The green curves show the number of G^* dissociation events which is the signal monitored by the experiment of Heck and Hofmann.

The total number of G^* dissociation events rise with the initial number of inactive G-proteins present on the vesicle. In contrast a decrease in the numer of back reactions from MetaII to MetaI (cyan curves) is visible with rising G-protein numbers.

Comparing the average number of G^* dissociation events with the predictions of the ODE model (red solid lines) reveals that the results from G10, G20 and G30 match almost perfectly to the mean of our trajectories. Together with G40, G50 and G60 all setups lie within the error bars. At the border of our simulated time of 100ms, the ODE description leaves the error bars of the G50 and G60 signals. An almost identical behavior can be found for the experimentally measured data (black

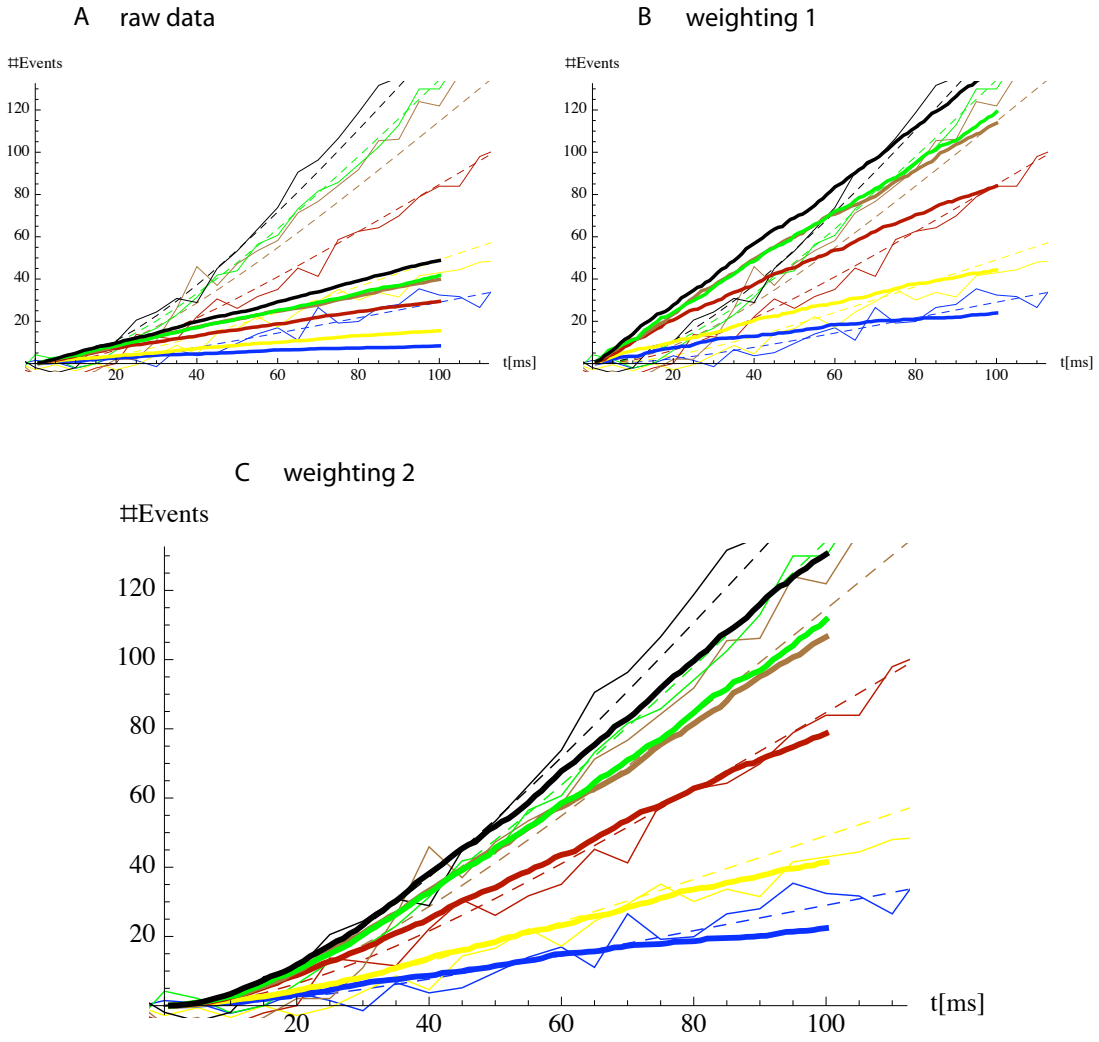

Figure 22: Postprocessing of the cumulative G* dissociation events of our simulated trajectories (bold lines) in comparison to experimental data (solid thin lines) and an ODE model description of the system (dashed thin lines). The colors indicate the different setups: G10 (blue), G20 (yellow), G30 (red), G40 (brown), G50 (green) and G60 (black). A indicates the raw simulation data in comparison to the experimental and ODE data. B depicts the same scenario but with the simulation data weighted by factor of $\frac{1}{0.35}$. C illustrates the simulation data after the second reweighting step according to the reaction probability of the MetaI to MetaII form of Rhodopsin.

solid line) in comparison with our simulation results.

In summary our simulation results are in a good aggreement with the experimental results and its ODE model description.

5.3 Spacial effects of explicit particle dynamics compared to the ODE model

In the following section the spacial effects that arise from G-protein depletion on the membrane are discussed.

5.3.1 Regimes of different expected behavior

During the time evolution of our model system, the initial pool of membrane bound G-protein is transformed into its active state and then dissociates from the membrane. The prerequisite of this transformation is that a G-protein meets the single active Rhodopsin on the vesicle via diffusional motion. However as the time evolves and the pool of inactive G-proteins becomes smaller and smaller, it becomes more and more unlikely that R^* and G find each other on the membrane.

The speed at which R^* and G can find each other is the sum of their diffusion constants $D_{R^*G} = 2\mu m^2 s^{-1}$. After each activation reaction of a G by R^* it takes a certain time for an other pair of reaction partners to find each other. Using the average <> of this waiting time t_{wait} gives us the possibility to compute the area that R^* and G can sample between two reactions to find each other. If the probability to find a G in this area is larger than one we are in a regime of well mixed conditions where the reaction partners can find each other very quickly and an ODE model description of the system seems appropriate. However if the probability to find a G drops below 1 we are in a regime where spatial effects play a role and the actual particle positions with respect to each other start to matter.

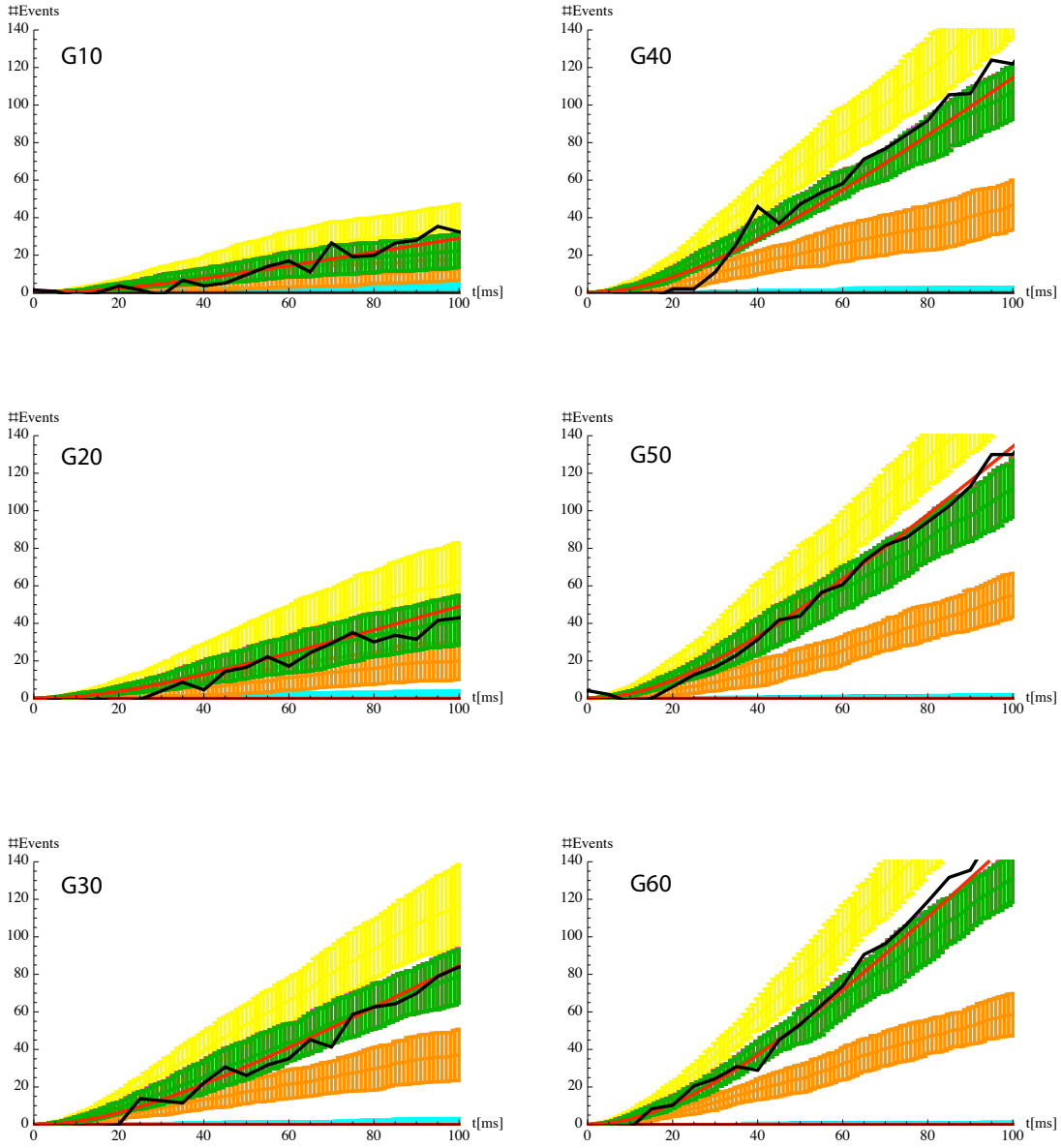

Figure 23: Average cumulative reaction events of all simulated setups from G10 to G60. The number of G^* dissociation events is depicted in green and is compare to the experimental data obtained from that setup (black solid line) and the curse of an ODE model derived from the experiments (red solid line). Please see Figure 19 for the color coding.

	G10	G20	G30	G40	G50	G60
G	21	40	88	156	228	335
$< t_{wait} > [ms]$	6.91	4.34	2.24	1.72	1.55	1.38
$A(t_{wait})$ $[\mu m^2]$	0.0139	0.0083	0.0045	0.0034	0.0031	0.0028
G_{crit}	4.44	7.44	13.72	17.93	19.91	22.38

Table 7: Thresholds for the boundary of the low density regimes for the different setups. G: Initial number of G proteins, $< t_{wait} >$: average waiting time between two successive R^*+G complex formation reactions, $A(t_{wait})$: Area on the sphere that R^* and G can sample together to find each other for a reaction, G_{crit}: The critical number of G-proteins left on the sphere below which the low density regime starts where spatial effects become predominant.

In Table 7 the average waiting times of the six different setups are given, together with the initial available number of G-proteins on the vesicle and the respective critical number of G-proteins below which we enter the low density regime. The resulting boundaries of the low density regime for the respective setups are illustrated in Figure 24. Here the cumulative number of G^* dissociation events in the experimental data and its ODE model are depicted, together with the respective boundary to the low density regime of the individual setups. A curve crossing the boundary indicates that more G is depleted than its critical number. Above the boundary the low density conditions apply for the system.

5.3.2 Decreased reaction rates within lower density regimes

Due to our limited simulation time we can only study two boundary crossing events within the trajectories of G10 and G20. If we draw the regime boundaries into our data (see Figure 25) we see that they cross the curves exactly in those points that separate two parts of different slopes. For G10 (the lower curve) the slope below the boundary is 0.28 and decreases above it by 41% to 0.17. For G20 (the upper curve) the effect is less pronounced but still present: The slope decreases from 0.49 by 19% to 0.40 after the boundary.

These effects are clearly an effect of spacial effects on the disc vesicle membrane. During the time course of a simulation the only variable parameter to affect the number of R^*+G complex formation reactions is the number of G proteins. The complex formation reaction rate and the number of R^* remains fixed during the simulation. Above the regime boundary the number of still available G-proteins becomes so low, that R^* and G need a longer time to find each other which slows

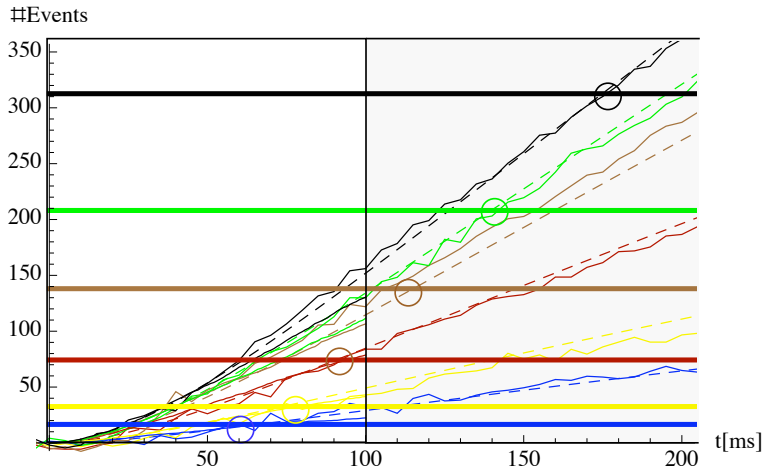

Figure 24: Cumulative number of G^* dissociation events in the experimental data (solid line) and its ODE model (dashed line). The colors indicate the different setups: G10 (blue), G20 (yellow), G30 (red), G40 (brown), G50 (green) and G60 (black). Boundary lines (parallel to the x axis) above which the critical regime starts are depicted in the same color as the respective setup configuration. The boundary crossings are marked by a small circles. The timescales that are not accessible by our simulation are shaded in grey.

down the number of complex formation reactions.

5.3.3 Increased reaction efficiency in lower density regimes

In the previous section we have seen that the low density of available G-protein on the vesicle surface can lower the cumulative number of produced G^* molecules. However the special spatial effects in the lower density regime can increase the efficiency of the first, R^*G complex formation reaction. At first this may sound contradictory but both are different effects. An increased reaction efficiency for complex formation may still lead to a lower output on G^* molecules if the now more efficient reaction can not find enough substrate to react.

The idea is the following: In the first regime there is plenty of G-protein available with which R^* can interact. If in this regime a just formed complex of R^* and G dissociates again, the G that has been in the complex before may still be in the neighborhood of R^* but the excessive supply of G-proteins renders it equally likely that R^* attempts a new complex formation with a new G-protein than with the old one. Yet this is not the case in the second regime where the G-protein supply is much lower. Here the probability that a dissociated R^*G-complex is formed again from its components after its dissociation is much higher.

We want to elaborate on this idea on the basis of kinetic data: If a complex between R^* and G has been formed it can dissociate again with rate $k_{-2} = 283\,s^{-1}$ or it can go on in the reaction chain and perform a nucleotide exchange with rate $k_3 = 607.5\,s^{-1}$ which can be considered as an irreversible step that finally leads to

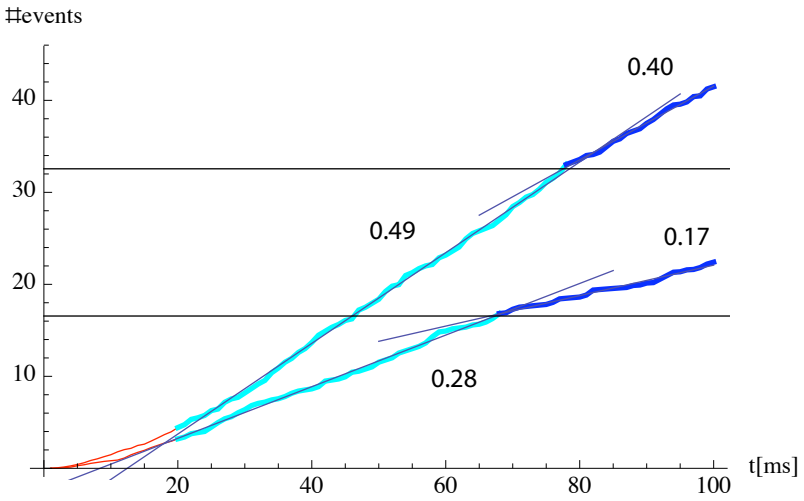

Figure 25: Average cumulative number of G^* dissociation events of our simulated data together with the boundaries of the low density regime for G10 (lower curve) and G20 (upper curve). The colors indicate the different regimes of high (cyan) and low (blue) G-protein density. The numbers indicate ths slopes of the respective linear fits of the G^* dissociation events. A clear decrease in reaction speed is visible from the high to the low density regimes.

the production of an activated Transducin G^*. Consequently the probability for a G-protein to be transformed into G^* is $p^+ = k_3/(k_{-2} + k_3) = 0.68$ while the probabiliy not to be transformed is $p^- = 0.32$.

If we now assume that the rebinding rate of a dissociated G is zero in the first regime, the G^* production efficiency of the reaction will remain $p^+ = 0.68$. However this is not the case for the second regime where such rebinding events are assumed to be more likely. We can try to estimate a magnitude of this effect like this: After a R^*G complex dissociation event, the expected waiting time τ between the next complex formation events is the inverse of of its reaction rate $k_3 = 20710.5\, s^{-1}$ which results in $\tau = 48\mu s$. R^* and G have now time τ to diffuse around and find each other again to attempt an other complex formation. We can model this process by assuming R^* to be immobile in the origin of our coordinate system and G now diffuses around it with diffusion constant $D = D_G + D_{R^*}$. The area of an R^* molecule is $A_{R^*} = 33nm^2$ and the area the G-protein can cover in time τ is $A_G = 97nm^2$. This means, that the probability that G collides again with R^* on its path is $p_{again} = \frac{A_G}{A_{R^*}} = 0.34$.

Now we can construct a markov jump process with two ordinary and one absorbing state. The states are 1: R^* and G are free, 2: R^*G in complex and 3: G^* and the transitions t_{ij} from state i to state j between them:

$$T = \begin{bmatrix} 0 & p_{again} & 0 \\ p^- & 0 & p^+ \\ 0 & 0 & 0 \end{bmatrix}$$

. This means that if we have a complex R^*G it can form either G^* $(2 \rightarrow 3)$ with

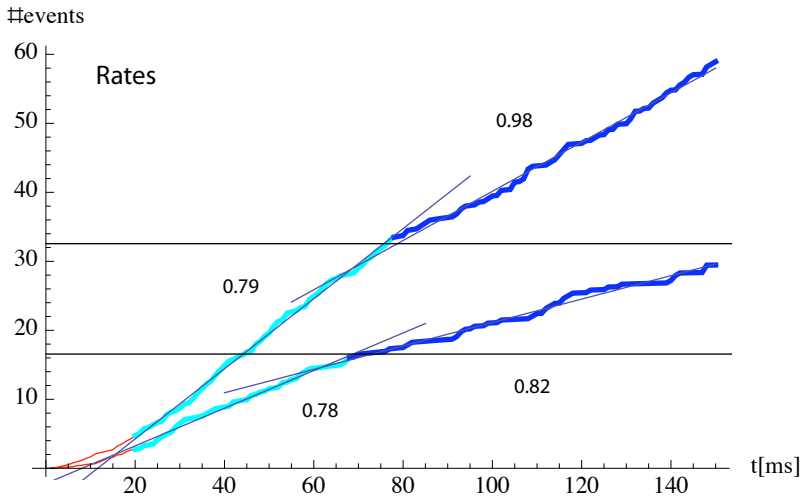

Figure 26: The same setup is depicted as in Figure 25 but with the difference that the simulation time here is 150ms instead of 100ms. Instead for the slopes of a linear fit, the numbers stand for the reaction rate at which an individual G-protein that meets an R^* is transformed to an G^*. This rate is increased in the low density regime.

probability $p+$ or it can dissociate again $(2 \rightarrow 1)$ with probability p^-. And since we are in the low density regime a third component enters with the possibility that the parts of a dissociated complex can make an other attempt to form a complex $(1 \rightarrow 2)$ with probabiilty p_{again}. Once the system has reached the absorbing state 3 it never leaves it.

This leads now to the following series of possible events: A complex forms and directly goes to state 3 with probability p^+, a complex forms then dissociates with probability p^- but associates again with p_{again} and then goes to state 3 which would in total have probability $P = p^+ + p^+ \times (p^- \times p_{again})$. Each time we run the circle of dissociation and association we get an $(p^- \times p_{again})$ component. In total we have the series: $P = p^+(1 + (p^- \times p_{again}) + (p^- \times p_{again})^2 + ... = p^+ \sum_{n=0}^{\infty}(p^- \times p_{again})^n$. In our case, P valuates to 0.77 which is an increase of 12% compared with the rate where no re-associations are assumed.

To test this hypothesis of an increased probability for individual G-protein to become activated in the low density regime, we tracked all G-proteins in our simulation individually and evaluated their attempts to form complexes with R^* and their successs in becoming activated. Unfortunately the 100ms trajectories that we used before did not provide us with enough statistics since the first regimes in G10 and G20 started at about 68ms and 78ms respectively. For this reason we generated eight new trajectories for each G10 and G20 with simulation time of 150ms. This was affordable since these trajectories have the smallest number of G-proteins which rendered a such long simulation for them to be relatively cheap in comparison. The 150ms trajectories are depicted in Figure 26together with the regime boundaries.

Table 8 shows that in both setup G10 and G20 the number of trials of a G-

	G10		G20	
	Regime1	Regime2	Regime1	Regime2
trials	68	38	134	63
successes	53	31	106	62
rate	0.78	0.82	0.79	0.98

Table 8: Number of G-proteins that attempted a complex formation with R^*, the number how many of them succeeded in becoming activated in the two different regimes of G10 and G20 and the rate that results from the fraction of trials and successes.

protein to become activated may decrease in the second regime of low density but their rate of success is increased. The number of trials indicate all individual G-proteins in the eight realizations of the respective setup, that attempted a comlex formation with R^*. If such a G-protein ended up in a R^*G_0 complex it is counted as a success. Here it doesnt matter for count as a success if the G-protein reached this final state directly or diffused away at first after a complex dissociaton, came back and succeded in an other attempt. We see from the analysis that the effect of increasing the turnover efficiency of an individual G is higher than expected from theoretical considerations. However the assumptions made there were, that in the high density regime no rebinding events occur while they would be favored in the low density regime. Under simulation conditions it seems plausible that rebinding already occurs in the first regime and is increased in the second one which leads to a shift to a higher efficiency in both regimes compared to the estimated ones.

The information, about the number of attempts an individual G-protein needed on average for a complex formation in each regime until it succeeded, could even more support the hypothesis of a higher probability of the R^* to catch the same G twice or more in the low density regime. Figure 27 depicts how many Gs succeeded in the first trial or after one or more dissociation and re-association events. To render the numbers of the two regimes comparable to each other they are normalized by the number of Gs that succeeded in their first trial. It is clearly visible, that the transition from the high (cyan) to the low (blue) density regime makes it more likely for an individual G-protein to get a second and even a third chance to succeed. The G-protein activation machinery handles its rare ressources more efficiently in the low density regime than it does when plenty of supply is available.

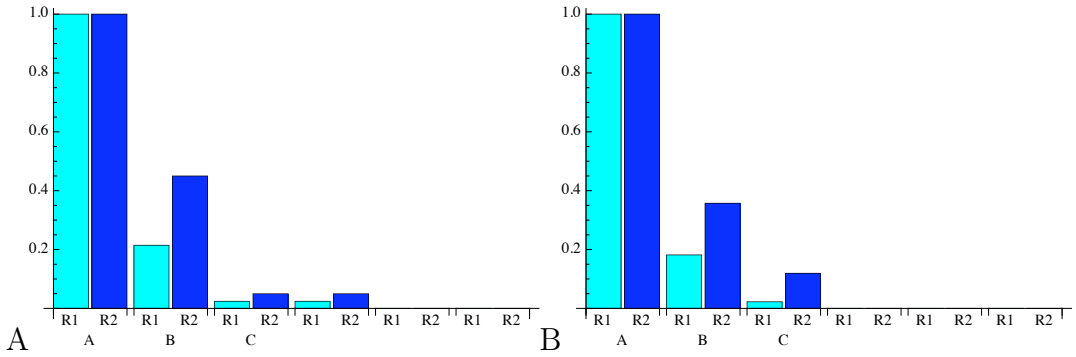

Figure 27: Numbers of G-proteins in the high (cyan) and low (blue) density regime that succeed in their first (A) trial to become part of an R^*G_0 complex or make a second attempt after a complex dissociation (B) or even make a third attempt (C). The numbers are normalized to the number of first trial successes. A on the left depicts setup G10, B on the right depicts setup G20. In the low density regimes more G-proteins get a second or even third chance to succeed.

6 Summary and conclusions

The obtained results have a number of interesting implications:

1. When diffusion is free and isotropic, i.e. no specific structures such as Rhodopsin oligomer bands (Ref [21]) are present, then the $G*$ production is not diffusion-limited. The diffusion-limited rate would be a factor of $\sim$8 faster than the experimentally measured rate under otherwise optimal conditions (plenty of GTP and no GDP in the solution). This statement is not necessarily true when Rhodopsin patterns do form on the disc memrane.

2. Fig. 23 shows the average $G*$ production of a single photon activation. This is an intermediate part of the single-photon response. In particular, this Figure also shows the variability between individual realizations. It is observed that the individual realization show very little variability, i.e. are very uniform. This is at first surprising since at this stage none of the effects that have so far been proposed as being responsible for the uniformity of the single-photon response are involved in our simulation. The uniformity of the $G*$ production is a simple consequence of the fact the it is the same single $R*$ that must iteratively go through exponentially distributed waiting times with means k_1^{-1} and k_2^{-1} for each $G*$ produced. Since the total number of $G*$ produced depends on the very same $R*$ going through this random process over and over again, it is simply the central limit theorem which leads to a small variation to the number N of $G*$ produced after a given time. In other words, even though the individual times a single $G*$ needs to be produced after it has formed a complex with $R*$ varies a lot, the total number of $G*$ produced by a single $R*$ after at least 3-5 such events is almost uniformly reproducible. Although this result does not explain the uniformity of the entire output current signal, it is

certainly directly correlated with the uniformity of the rise of this current.

3. Fig. 23 also shows the comparison between our simulated trajectories and the experimental data suggests, that we can explain the available kinetic data with our explicit particle diffusion model. Furthermore the high similarity between the predictions of an ODE model and our data suggests that we have well mixing conditions on our disc vesicles, at least for certain regimes of parameters. The low difference between the computed microscopic diffusion constant and the observable macroscopic value, which indicates low crowding effects, even more supports this hypothesis of well mixed conditions. We find this regime whenever the number of available G-proteins on a vesicle is high enough that R^* can immediately find a new G after the release of a G^*. We call this regime the high density regime. However to study the dynamics in this regime, an ODE description of the system is sufficient and the full particle resolution can be neglected. Yet it states a proof of concept that the full particle resolution leads to the same results.

4. In our data we see that the well mixed density regime does not extend throughout the entire parameter space. If the G-protein concentration drops below a certain threshold during the time course of the reactions, well mixing can no longer be assumed. Now the explicit particle positions with respect to each other start to matter and influence the dynamic significantly. One example for such spatially influenced behavior is the drop in G^* dissociation speed by 20% to 40%, immediately after the number of G-proteins has dropped below the threshold that separates the high from the low density regime (see Figure 25). Under low density conditions it takes the R^* longer times to find G-proteins which slows down the output rate. An other effect of spatial influence of particle positions with respect to each other is the increase in G turnover efficiency for individual G-proteins in the low density regime. Table 8 shows that the individual success rate of a G to become activated is increased by 5% to 24% leading to individual G activation probabilities of up to 98%. This can be explained by the assumption that, because of less competition between individual Gs for the receptor in the low density regime, individual Gs get multiple chances to become activated even if a first attempt of complex formation failed. Figure 27 shows that the distribution of attempt numbers, after which individual Gs succeed in becoming activated, is shifted towards higher number of attempts in the low density regime. Such effects are exactly the reason why single particle resolution is important even in systems which seem to be well mixed on first glance. Every attempt to capture spatial effects like those mentioned with models that assume well mixing in different subvolumes or even the entire system will most probably fail.

5. Though our medhod could describe the experimental data quite well and reavealed some spatial effects in addition, it still remains based on the assumption of free diffusion of all particle species without any attraction potentials that were proposed to be present under physiological conditions (such as

Rhodopsin-Rhodopsin attraction driven oligomer band formation on the disc membrane [21]). Our presented model can be considered to be a maximum model with respect to the freedom of particles. This can also be seen as a reason for the success of an ODE model description for our system, at least in the regime of high G-protein density. Yet first experiments with Rhodopsin-Rhodopsin attraction potentials (see Section 7.1) show, that even a slight attractive potential would have a significant global effect on the patterns and the dynamics of the entire disc, and thus likely on the entire phototransduction cascade. It is conceivable that such potentials do exist but depend on the conformational state of Rhodopsin. For example, inactive Rhodopsin may have a negligible attraction potential, thus yielding a situation where the free-diffusion setup can be made fully consistent with the measurements in [27], but in other conformational states Rhodopsin may have significant interaction potentials. Such a setting could be useful for molecular sorting on the disc membrane that would effectively deposit Ligand-free Opsins in "dead clusters", thus freeing diffusion space for the remaining Rhodopsins that can then still work efficiently. In any case, additional attraction potentials, that may even lead to the formation of patterns, will increase the effect of crowding and will therefore enlarge the regime where spatial effects matter. The study of these effects present the outlook of this work.

7 Outlook

In this section an outlook of planned further research, based on this work is presented. Parts of this work are already under investigation, as the effect of Rhodopsin-Rhodopsin attraction potentials and its resulting effects, others are planned for the near future.

7.1 Free diffusion versus pattern formation of Rhodopsins

A number of recent studies have discussed the possibility of the formation of patterns or anisotropic structures of Rhodopsins on the disc membrane [32, 19, 18, 23, 30, 52, 42]. Although the physiological relevance of these observations is debated due to the possible bias resulting from necessities in the experimental or simulation setup [11], it is worthwhile to study and understand the effects - if any at all - that pattern formation would have on the function of the phototransduction activation module. Ref [13] has suggested that the existence of diffusion obstacles strongly affect the overall transport on the disk, but these studies were done using a grid-based Monte Carlo procedure and did not involve physically realistic molecular diffusion and interaction properties. Here, we have compared the vesicle dynamics using two different Rhodopsin-Rhodopsin interaction potentials. In setup A (Table 6), a purely repulsive potential was used to exclude interpenetration of proteins on the membrane, but otherwise diffusion was free, using microscopic diffusion constants that would upon crowding effects reproduce the experimentally-determined macroscopic diffusion constants of Rhodopsin and Transducin [43]. In setup B (Table 6), Rhodopsins were given a potential that makes them additionally to the repulsive core slightly attract other Rhodopsins at nearby distances (see Fig. 8 for illustration). The relevance of such a potential is supported in particular by [30, 42], although further quantitative studies are required to determine the magnitude and orientational dependence of the potential. Both simulations were started from a uniformly random assignment of protein positions on the membrane. While the setup A simulations as expected maintain a homogeneous and isotropic distribution of proteins on the membrane, setup B simulations quickly (with few μs simulation time) converge to aggregates or clusters of Rhodopsins of a typical size (Fig. 28a and b). The corresponding radial distribution functions (rdf) between Rhodopsins are shown in Fig. 28c and d. While the rdf of the purely repulsive potential mainly shows depletion of particles below the collision distance with a osciallatory structure at longer distances that converges towards the mean particle density, the rdf of the attractive-repulsive potential has significantly more pronounced structures. Fig. 28d shows also the resemblance of this rdf with the rdf of a crystalline structure that was obtained by densely packing the vesicle surface with Rhodopsins using purely repulsive potentials. Dynamically, it is observed that the macroscopic diffusion of Rhodopsins in the attractive-repulsive case is strongly slowed down. This slowdown is more pronounced for stronger attractiveness in the potential, because of two additive effects: (i) for stronger attractive potentials, the exchange of Rhodopsins between clusters becomes more rare, reducing the contribution to the macroscopic diffusion constants

by single Rhodopsin escapes, and (ii) the average cluster size increases, as the favorable enthalpy loss upon cluster formation outweighs the unfavorable entropy loss, and large clusters diffuse more slowly than small clusters. For any but very shallow interaction potentials, the experimentally-measured macroscopic diffusion constants could only be achieved with extremely large microscopic diffusion constants that are untypical for membrane proteins in lipid solution. This suggests that the attractive interaction between inactive Rhodopsins must be weak, if it exists at all. However, this does not exclude the existence of strong attractive potentials for Rhodopsins in other than the inactive states and further quantitative studies are needed here.

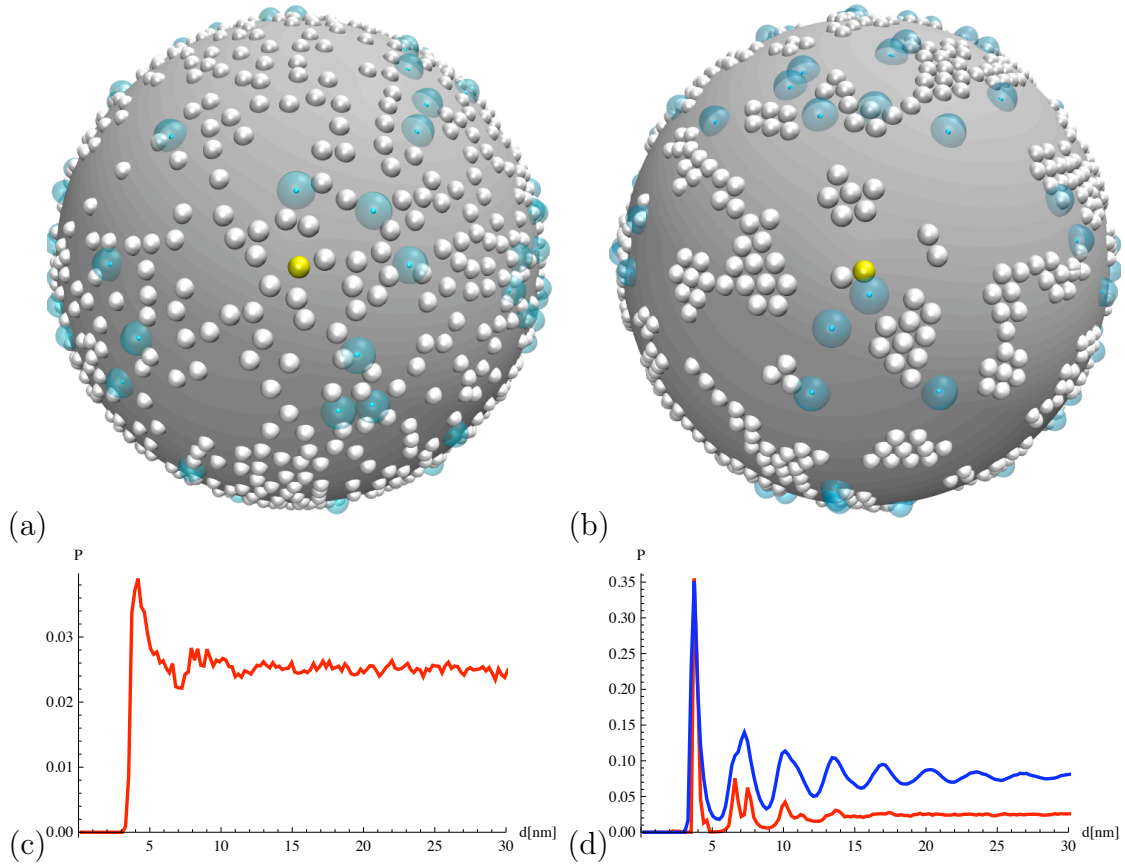

Figure 28: The effect of an attractive Rhodopsin-Rhodopsin potential. (a) Representative simulation snapshot of the vesicle with a purely repulsive interaction potential, showing the active Rhodopsin (yellow), inactive Rhodopsins (white) and Transducins (cyan). (b) Representative simulation snapshot with attractive Rhodopsin-Rhodopsin potential. (c) Radial distribution function between Rhodopsins for purely repulsive interaction potential. (d) Radial distribution function between Rhodopsins with attractive potential (red), compared with a radial distribution function that has been obtained for a crystalline-like dense packing of Rhodopsins on a sphere (blue).

7.2 Suggested future work

Deeper investigation of the data provided by Heck and Hofmann The experimental data used in this work is only a fraction of the data Heck and Hofmann measured and published in [27]. Here we only used G-protein titration data under constant nucleotide concentrations of GDP and GTP. Additional to that GDP and GTP titration data exist as well for the same experimental setup. The inclusion of these data sets in our model will provide further insight whether the "free diffusion model" (using no other interactions than purely repulsive potentials between particles) can explain the entirety of these measurements, or whether additional effects are needed. Additionally the effect of different nucleotide concentrations on the boundary between a well mixed and a single molecule regime have to be investigated.

Theoretical study of Rhodopsin-Rhodopsin interaction potentials: A prerequisite for the study of Rhodopsin dimerization or even oligormerization is the use of reliable interaction potentials. As already indicated in 7.1 a high potential attractiveness may lead to a pronounced pattern formation as it has been seen in [21] but lead on the other hand to atypical very high microscopic diffusion constants to still provide a certain mobility on the membrane. Additional insight into this question could come from coarse-grained molecular dynamics simulations (similar to the setup in [42] but with more extensive sampling and different Rhodopsin structures, e.g. [41]) and experiments (e.g. [30]). It is planed for the future to obtain such data and to include them into the simulation.

Transition from homogenous to more complicated diffusional systems The present study models only the very first steps in the light induced photoactivation cascade of the Rod cell. It is planned for the future to extend the knowledge about particle dynamics simulations to larger systems of size of the entire Rod outer segment (ROS) where the full cascade could be investigated including as well all activation as all shut-down reactions. This extension will bring additional spatial effects because of the special geometry of layered discs hosting 2D diffusion which are themselves embedded into the 3D space of the surrounding cytoplasm. Extensive work will have to be done in order to finally come up with a full particle resolution model of the ROS but the possible outcomes are promising and the present study states already the first step in this direction.

References

[1] M Ander, P Beltrao, B Di Ventura, and J Ferkinghoff-. . . . Smartcell, a framework to simulate cellular processes that combines stochastic approximation with diffusion and localisation: analysis of simple networks. *Syst. Biol*, 1(1):129–138, Jan 2004.

[2] D Andreucci, P Bisegna, G Caruso, HE Hamm, and E DiBenedetto. Mathematical model of the spatio-temporal dynamics of second messengers in visual transduction. *Biophysical Journal*, 85(3):1358–1376, 2003.

[3] S Andrews and D Bray. Stochastic simulation of chemical reactions with spatial resolution and single molecule detail. *Physical biology*, 1:137–151, Jan 2004.

[4] Peter Atkins and Julio dePaula. Physikalische chemie. *Wiley-VCH, Weinheim*, 2009.

[5] W Baehr and P Liebman. Visual cascade. *Encyclopedia of Life Sciences (http://www. els. net or http://retlna. hmbg. utah. edu)*, 2001.

[6] P Bisegna, G Caruso, D Andreucci, L Shen, VV Gurevich, HE Hamm, and E DiBenedetto. Diffusion of the second messengers in the cytoplasm acts as a variability suppressor of the single photon response in vertebrate phototransduction. *Biophysical Journal*, 94(9):3363–3383, 2008.

[7] G Broderick, M Ru'aini, E Chan, and M Ellison. A life-like virtual cell membrane using discrete automata. *In silico biology*, 5:163–178, Jan 2005.

[8] ME Burns and VY Arshavsky. Beyond counting photons: trials and trends in vertebrate visual transduction. *Neuron*, 48(3):387–401, 2005.

[9] ME Burns and TD LAMB. 1 u visual transduction by rod and cone photoreceptors. *The visual neurosciences*, page 215, 2004.

[10] G Caruso, P Bisegna, L Shen, D Andreucci, HE Hamm, and E DiBenedetto. Modeling the role of incisures in vertebrate phototransduction. *Biophysical Journal*, 91(4):1192–1212, 2006.

[11] M Chabre, R Cone, and H Saibil. Biophysics (communication arising): Is rhodopsin dimeric in native retinal rods? *Nature*, Jan 2003.

[12] M Covert, E Knight, J Reed, and M Herrgard. Integrating high-throughput and computational data elucidates bacterial networks. *Nature*, 429:92–96, Jan 2004.

[13] D Dell'Orco and H Schmidts. Mesoscopic monte carlo simulations of stochastic encounters between photoactivated rhodopsin and transducin in disc membranes. *J. Phys. Chem. B*, 112(14):4419–4426, 2008.

[14] R Drzymala, H Weiner, C Dearry, and P Liebman. A barrier to lateral diffusion of porphyropsin in necturus rod outer segment disks. *Biophysical Journal*, 45:683–692, Jan 1984.

[15] M Elowitz, A Levine, E Siggia, and P Swain. Stochastic gene expression in a single cell. *Science*, 297(5584):1183–1186, Jan 2002.

[16] Radek Erban and S Jonathan Chapman. Stochastic modelling of reaction-diffusion processes: algorithms for bimolecular reactions. *Physical Biology*, 6(4):046001, 2009.

[17] S Felber, HP Breuer, F Petruccione, J Honerkamp, and KP Hofmann. Stochastic simulation of the transducin gtpase cycle. *Biophysical Journal*, 71(6):3051–3063, 1996.

[18] D Fotiadis, B Jastrzebska, and A Philippsen. Structure of the rhodopsin dimer: a working model for g-protein-coupled receptors. *Current opinion in ...*, Jan 2006.

[19] D Fotiadis, Y Liang, S Filipek, DA Saperstein, A Engel, and K Palczewski. Atomic-force microscopyrhodopsin dimers in native disc membranes. *Nature*, 421(6919):127–128, 2003.

[20] Dimitrios Fotiadis, Beata Jastrzebska, Ansgar Philippsen, Daniel J. Müller, Krzysztof Palczewski, and Andreas Engel. Structure of the rhodopsin dimer: a working model for g-protein-coupled receptors. *Current opinion in structural biology*, 16(2):252–259, April 2006.

[21] Dimitrios Fotiadis, Yan Liang, Slawomir Filipek, David A. Saperstein, Andreas Engel, and Krzysztof Palczewski. Atomic-force microscopy: Rhodopsin dimers in native disc membranes. *Nature*, 421(6919):127–128, January 2003.

[22] DT Gillespie. Exact stochastic simulation of coupled chemical reactions. *The journal of physical chemistry*, 81(25):2340–2361, 1977.

[23] VI Govardovskii, DA Korenyak, SA Shukolyukov, and LV Zueva. Lateral diffusion of rhodopsin in photoreceptor membrane: a reappraisal. 2009.

[24] RD Hamer, SC Nicholas, D Tranchina, TD Lamb, and JLP Jarvinen. Toward a unified model of vertebrate rod phototransduction. *Visual neuroscience*, 22(04):417–436, 2005.

[25] RD Hamer, SC Nicholas, D Tranchina, PA Liebman, and TD Lamb. Multiple steps of phosphorylation of activated rhodopsin can account for the reproducibility of vertebrate rod single-photon responses abbreviations used in this paper: Arr, arrestin; pde, phosphodiesterase; rk, rhodopsin kinase; spr, single-photon response. *Journal of General Physiology*, 122(4):419–444, 2003.

[26] J Hattne, D Fange, and J Elf. Stochastic reaction-diffusion simulation with mesord. *Bioinformatics*, 21(12):2923–2924, Jan 2005.

[27] M Heck and KP Hofmann. Maximal rate and nucleotide dependence of rhodopsin-catalyzed transducin activation - initial rate analysis based on a double displacement mechanism. *Journal of Biological Chemistry*, 276(13):10000–10009, Jan 2001.

[28] K Hofmann, P Scheerer, and P Hildebrand. Ag protein-coupled receptor at work: the rhodopsin model. *Trends in Biochemical ...*, Jan 2009.

[29] Murray J. Mathematical biology. *Berlin: Springer*, 2002.

[30] B Jastrzebska, T Maeda, L Zhu, and D Fotiadis. Functional characterization of rhodopsin monomers and dimers in detergents. *J Biol Chem*, 279:54663–54675, 2004.

[31] Tai-Yang Kim, Hiroshi Uji-i, Martina Möller, Benoit Muls, Johan Hofkens, and Ulrike Alexiev. Monitoring the interaction of a single g-protein key binding site with rhodopsin disk membranes upon light activation. *Biochemistry*, 48(18):3801–3803, May 2009.

[32] Tai-Yang Y. Kim, Hiroshi Uji-i, Martina Möller, Benoit Muls, Johan Hofkens, and Ulrike Alexiev. Monitoring the interaction of a single g-protein key binding site with rhodopsin disk membranes upon light activation. *Biochemistry*, 48(18):3801–3803, May 2009.

[33] TD Lamb. Stochastic simulation of activation in the g-protein cascade of phototransduction. *Biophysical Journal*, 67(4):1439–1454, 1994.

[34] TD Lamb. Gain and kinetics of activation in the g-protein cascade of phototransduction. *Proceedings of the National Academy of Sciences*, 93(2):566–570, 1996.

[35] TD Lamb. Phototransduction in vertebrate rods and cones: molecular mechanisms of amplification, recovery and light adaptation. *Handbook of biological physics*, 3, 2000.

[36] TD Lamb and EN Pugh. A quantitative account of the activation steps involved in phototransduction in amphibian photoreceptors. *The Journal of Physiology*, 449(1):719–758, 1992.

[37] Hazime Mori. Transport, collective motion, and brownian motion. *Progress of Theoretical Physics*, 33(3):423–455, 1965.

[38] S Nickell, P Park, W Baumeister, and K Palczewski. Three-dimensional architecture of murine rod outer segments determined by cryoelectron .... *Journal of Cell Biology*, Jan 2007.

[39] S Nikonov, T LAMB, and E Pugh Jr. The role of steady phosphodiesterase activity in the kinetics and sensitivity of the light-adapted salamander rod photoresponse. *Journal of General Physiology*, 116(6):795–824, Jan 2000.

[40] K Palczewski. G protein–coupled receptor rhodopsin. *Annual Reviews*, 75:743–767, Jan 2006.

[41] Jung Hee Park. Crystal structure of the ligand-free g-protein-coupled receptor opsin. *Nature*, 454:183–187, 2008.

[42] Xavier Periole, Thomas Huber, Siewert-Jan Marrink, and Thomas P. Sakmar. G protein-coupled receptors self-assemble in dynamics simulations of model bilayers. *Journal of the American Chemical Society*, 129(33):10126–10132, August 2007.

[43] EN PUGH and TD LAMB. Amplification and kinetics of the activation steps in phototransduction, Jan 1993.

[44] A Rahman and F Stillinger. Molecular dynamics study of liquid water. *Phys. Rev.*, 55:3336, 1971.

[45] D Ridgway, G Broderick, and M Ellison. Accommodating space, time and randomness in network simulation. *Current opinion in biotechnology*, 17:493–498, Jan 2006.

[46] R Rodieck and R Rodieck. The first steps in seeing. *Sinauer Associates, Inc. / Publishers Sunderland, Massachusetts*, Jan 1998.

[47] Chandrasekhar S. Stochastic problems in physics and astronomy. *Rev. Mod. Phys*, 15:2–89, 2008.

[48] C Sanford, M Yip, C White, and J Parkinson. Cell++–simulating biochemical pathways. *Bioinformatics*, 22:2918–2925, Jan 2006.

[49] B Slepchenko, J Schaff, I Macara, and L Loew. Quantitative cell biology with the virtual cell. *Trends in cell biology*, 13(11):570–576, Jan 2003.

[50] J Stiles, T Bartol Jr, and E Salpeter. Monte carlo simulation of neurotransmitter release using mcell, a general simulator of cellular physiological processes. *Computational Neuroscience*, pages 87–127, Jan 1998.

[51] VanKampen. Stochastic processes in physics and chemistry. *Amsterdam, London, New York: Elsevier*, 1992.

[52] Q Wang, X Zhang, L Zhang, F He, G Zhang, M Jamrich, and T. G Wensel. Activation-dependent hindrance of photoreceptor g protein diffusion by lipid microdomains. *Journal of Biological Chemistry*, 283(44):30015–30024, Aug 2008.

[53] T Wensel. Signal transducing membrane complexes of photoreceptor outer segments. *Vision research*, 48:2052–2061, Jan 2008.

[54] C Wey, R Cone, and M Edidin. Lateral diffusion of rhodopsin in photoreceptor cells measured by fluorescence photobleaching and recovery. *Biophysical Journal*, 33:225–232, Jan 1981.

[55] Robert Zwanzig. Nonlinear generalized langevin equations. *Journal of Statistical Physics*, 9:215–220, 1973. 10.1007/BF01008729.

8 Appendix

8.1 Derivation of microscopic vs macroscopic reaction rates in 2D

In order to derive a formula that incorporates microscopic and macroscopic reaction rates in two dimensions we consider the diffusion of a molecular species A to a disc with radius $\hat{r}$ which removes molecules of A with the rate λ. Let the center of the disc be at the origin.

To describe this system, we start from the Laplacian Diffusion Equation

$$\frac{\mathrm{d}c(x,t)}{\mathrm{d}t} = D\nabla^2 c(x,t) \tag{9}$$

which relates the change in time of the molecular concentration of A $c(x,t)$, given at a point x in space and time t, to the diffusion constant D. If we assume the movement of both entities, the disc and molecules of A, D becomes the sum of both diffusion constants $D = D_A + D_B$.

To use the symmetry of the system we express this equation in therms of polar coordinates

$$\frac{\mathrm{d}c(r,\theta,t)}{\mathrm{d}t} = D\nabla^2 c(r,\theta,t), \tag{10}$$

with x being expressed now in terms of the distance from the origin r and the angle θ. Remark that the Laplacian Operator ∇^2 has now to be expressed in polar coordinates as well, which reads

$$\nabla^2 = \frac{\partial^2}{\partial r^2} + \frac{1}{r}\frac{\partial}{\partial r} + \frac{1}{r^2}\frac{\partial^2}{\partial \theta^2}. \tag{11}$$

Because of the isotropy of the system, the angle θ makes no difference which simplyfies the Laplacian to

$$\nabla^2 = \frac{\partial^2}{\partial r^2} + \frac{1}{r}\frac{\partial}{\partial r}. \tag{12}$$

If we apply the Laplacian to the Diffusion Equation we get

$$\frac{\mathrm{d}c(r,t)}{\mathrm{d}t} = D\left[\frac{\partial^2 c(r,t)}{\partial r^2} + \frac{1}{r}\frac{\partial c(r,t)}{\partial r}\right], \tag{13}$$

which evaluates to

$$\frac{\partial^2 c(r,t)}{\partial r^2} + \frac{1}{r}\frac{\partial c(r,t)}{\partial r} - \frac{1}{D}\frac{\partial c(r,t)}{\partial t} = 0. \tag{14}$$

In our system, the change in concentration over time $\frac{\partial c(r,t)}{\partial t}$ splits into two cases:

1. Outside the disc, $c(r,t)$ equals the equilibrium concentration of A and remains constant:
$$\frac{\partial c(r,t)}{\partial t} = 0 \qquad for \quad r \geq \hat{r} \tag{15}$$

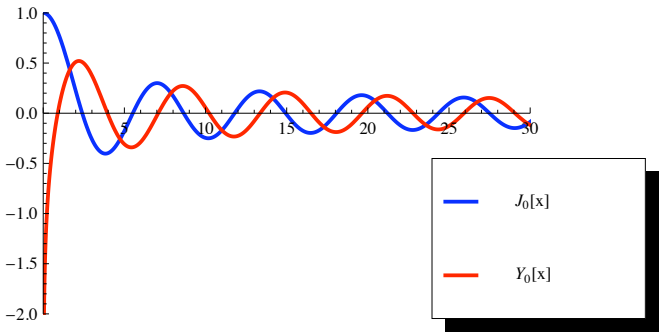

Figure 29: Bessel functions of the first (blue) and second kind (red) respectively.

2. Inside the disc of radius $\hat{r}$, molecules of A are removed with rate λ:

$$\frac{\partial c(r,t)}{\partial t} = \lambda c(r,t) \qquad for \quad r \leq \hat{r} \tag{16}$$

This leads to the following second order ODEs.

$$\frac{\partial^2 c}{\partial r^2} + \frac{1}{r}\frac{\partial c}{\partial r} = 0 \qquad for \quad r \geq \hat{r} \tag{17}$$

$$\frac{\partial^2 c}{\partial r^2} + \frac{1}{r}\frac{\partial c}{\partial r} - \frac{\lambda c}{D} = 0 \qquad for \quad r \leq \hat{r} \tag{18}$$

The general solution of these equations can be written in the following form:

$$c(r) = a_1 + a_2 log(r) \qquad for \quad r \geq \hat{r} \tag{19}$$

$$c(r) = a_3 J_0\left[\frac{ir\sqrt{\lambda}}{\sqrt{D}}\right] + a_4 Y_0\left[-\frac{ir\sqrt{\lambda}}{\sqrt{D}}\right] \qquad for \quad r \leq \hat{r} \tag{20}$$

$J_0[x]$ and $Y_0[x]$ denote here the Bessel function of the first and the second kind respectively.

To resolve the parameters a_1, a_2, a_3 and a_4 we use the the boundary conditions $\lim_{r\to 0} c(r)$ and $\lim_{r\to\infty} c(r)$ as well as the continuity of $c(r)$ and its derivative at $r = \hat{r}$.

1. $\lim_{r\to\infty} c(r) \stackrel{!}{=} const$ implies, that $a_2 = 0$ because otherwise $log(r)$ would the function cause to diverge. Furthermore $a_1 = c_\infty$, the value of the equilibrium concentration of A.

2. $\lim_{r\to 0} c(r) \stackrel{!}{=} const$ implies, that $a_4 = 0$ because otherwise $Y_0[x]$ would the function cause to diverge.

The application of these boundary conditions leads to the following equations:

$$c(r) = c_\infty \qquad for \quad r \geq \hat{r} \tag{21}$$

$$c(r) = a_3 J_0 \left[\frac{ir\sqrt{\lambda}}{\sqrt{D}} \right] \qquad for \quad r \leq \hat{r} \tag{22}$$

If we use now the condition of continuity at $r = \hat{r}$ we get

$$c_\infty = a_3 \tag{23}$$

$$a_3 = c_\infty J_0 \left[\frac{i\hat{r}\sqrt{\lambda}}{\sqrt{D}} \right]^{-1} \tag{24}$$

When now trying to apply the condition of continuity of the first derivative we have to derive both conditions and equate them:

$$c'(r) = 0 \qquad for \quad r \geq \hat{r} \tag{25}$$

$$c'(r) = -\, a_3 \frac{i\sqrt{\lambda}}{\sqrt{D}} J_1 \left[\frac{ir\sqrt{\lambda}}{\sqrt{D}} \right] \qquad for \quad r \leq \hat{r} \tag{26}$$

$$0 = -a_3 \frac{i\sqrt{\lambda}}{\sqrt{D}} J_1 \left[\frac{i\hat{r}\sqrt{\lambda}}{\sqrt{D}} \right] \tag{27}$$

Continuity of the first derivative is only given at the extreme points of the Bessel function which would imply, that we would constrain our choice of $\hat{r}$, λ or D such that we match such an extreme point. To allow for arbitrary choices we drop the continuity of the first derivative while pointing to the fact, that the ODEs that we constructed contain a jump by construction, namely the jump from 15 to 16. This jump can happen to be rather extreme, dependent on the choice of c_∞ and λ. This argument underlines why we cannot expect to have continuity of the first derivative at the jump side.

Referring to [16] the flux through the unit area of the boundary of the disc can be computed by

$$D \, \frac{\partial c}{\partial r}|_{r=\hat{r}} = -D \; a_3 \frac{i\sqrt{\lambda}}{\sqrt{D}} J_1 \left[\frac{i\hat{r}\sqrt{\lambda}}{\sqrt{D}} \right]. \tag{28}$$

The circumference of a disc is $2\pi\hat{r}$ which leads to the fact, that the total flux through the disc boundary is

$$-2\pi\hat{r} \; D \; a_3 \frac{i\sqrt{\lambda}}{\sqrt{D}} J_1 \left[\frac{i\hat{r}\sqrt{\lambda}}{\sqrt{D}} \right], \tag{29}$$

which gives with a_3,

$$-2\pi\hat{r}\ D\ \left(c_\infty J_0\left[\frac{i\hat{r}\sqrt{\lambda}}{\sqrt{D}}\right]^{-1}\right)\frac{i\sqrt{\lambda}}{\sqrt{D}}J_1\left[\frac{i\hat{r}\sqrt{\lambda}}{\sqrt{D}}\right]. \tag{30}$$

This quantity is equal to the rate constant of bimolecular reaction k multiplied by the concentration of the chemical far from the reacting molecule c_∞. Dividing by c_∞ we get the final result that relates the macroscopic rate k $[\frac{m^2}{s}]$with the microsopic rate $\lambda[\frac{1}{s}]$.

$$k = -2\pi\hat{r}\ D\ \frac{i\sqrt{\lambda}}{\sqrt{D}}\ \frac{J_1\left[\frac{i\hat{r}\sqrt{\lambda}}{\sqrt{D}}\right]}{J_0\left[\frac{i\hat{r}\sqrt{\lambda}}{\sqrt{D}}\right]} \tag{31}$$

The imaginary unit cancels out since the fraction of the two Bessel functions is only imaginary what leaves us with the following formula:

$$k = 2\pi\hat{r}\ \sqrt{D}\ \sqrt{\lambda}\ \frac{I_1\left[\frac{\hat{r}\sqrt{\lambda}}{\sqrt{D}}\right]}{I_0\left[\frac{\hat{r}\sqrt{\lambda}}{\sqrt{D}}\right]} \tag{32}$$